HHS Public Access

Author manuscript

Cell Rep Phys Sci. Author manuscript; available in PMC 2025 September 17.

Published in final edited form as:

Cell Rep Phys Sci. 2025 August 20; 6(8): . doi:10.1016/j.xcrp.2025.102779.

Revealing the catalytic mechanism of the Fe(II)/2-oxoglutarate-dependent human epigenetic modifying enzyme ALKBH5

Fathima Hameed Cherilakkudy[1], **Midhun George Thomas**[1], **Ann Varghese**[1], **Sodiq O. Waheed**[1], **Anandhu Krishnan**[1], **Vincenzo Venditti**[2], **Christopher J. Schofield**[3], **Deyu Li**[4], **Christo Z. Christov**[1], **Tatyana G. Karabencheva-Christova**[1,5,*]

[1]Department of Chemistry, Michigan Technological University, Houghton, MI 49931, USA

[2]Department of Chemistry, Iowa State University, Ames, IA 50011, USA

[3]Chemistry Research Laboratory, Department of Chemistry and the Ineos Oxford Institute for Antimicrobial Research, University of Oxford, Oxford OX1 3TA, UK

[4]Department of Biomedical and Pharmaceutical Sciences, College of Pharmacy, University of Rhode Island, Kingston, RI 02881, USA

[5]Lead contact

SUMMARY

ALKBH5 is one of only two known human non-heme Fe(II)/2-oxoglutarate-dependent oxygenases that catalyze the demethylation of N^6-methyladenine (m^6A) in single-stranded mRNA, underscoring its role in diverse cancers. Unlike its homolog, the fat mass and obesity-associated protein (FTO), which oxidizes m^6A to a stable N^6-hydroxymethyladenine (hm^6A) intermediate, ALKBH5 demethylates m^6A, yielding adenine and formaldehyde as products. Here, we integrate molecular dynamics simulations and quantum mechanics/molecular mechanics methods to elucidate ALKBH5's complete catalytic mechanism. Two post-hydroxylation pathways were evaluated: a proton transfer pathway and a Schiff base formation pathway, with the former emerging as the favored mechanism. We identify second-sphere residues Lys132 and Tyr139 as essential contributors to catalysis and demonstrate how Val191 and Tyr133 modulate activity. Dynamic analyses reveal that correlated motions of structural elements such as nucleotide recognition lids NRL1 and NRL2 and increased flexibility of the NRL2 loop in the hm^6A intermediate may be critical for efficient demethylation.

In brief

*Correspondence: tatyanak@mtu.edu.

AUTHOR CONTRIBUTIONS

Conceptualization, T.G.K.-C.; methodology, T.G.K.-C. and F.H.C.; investigation and formal analysis, F.H.C.; writing – original draft, F.H.C.; writing – review and editing, F.H.C., M.G.T., A.V., S.O.W., A.K., T.G.K.-C., C.Z.C., V.V., C.J.S., and D.L.; funding acquisition, T.G.K.-C.; supervision, T.G.K.-C. and C.Z.C.

DECLARATION OF INTERESTS

The authors declare no competing interests.

Cherilakkudy et al. reveal the catalytic mechanism ofALKBH5, with emphasis on dioxygen activation, substrate oxidation, and post-hydroxylation. Furthermore, the study explores the role of correlated motions and SCS residues in catalysis.

Graphical Abstract

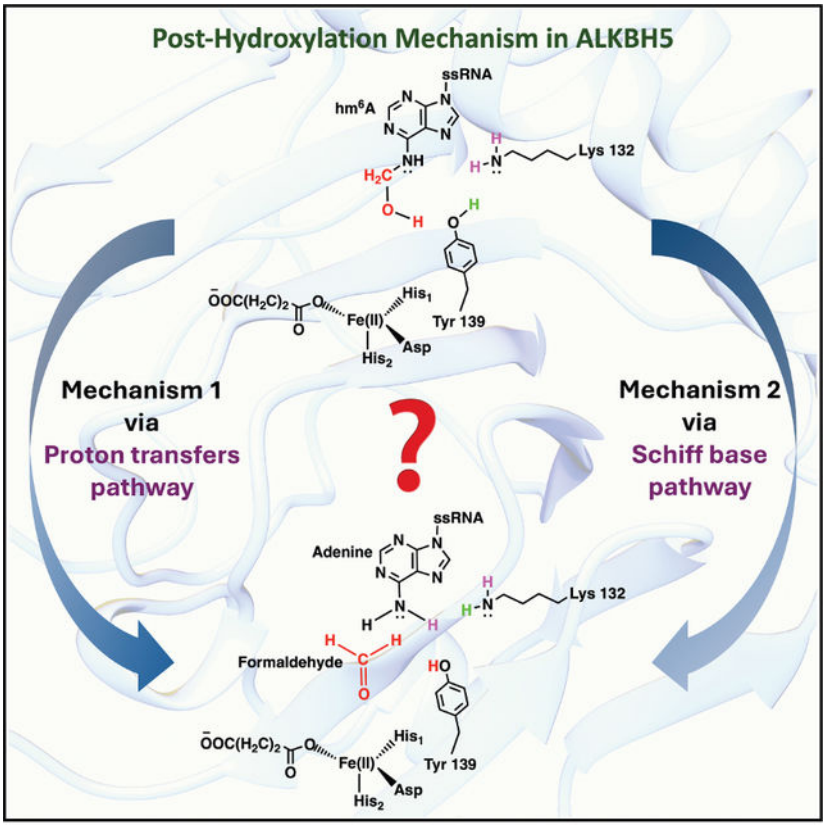

INTRODUCTION

The human RNA demethylase ALKBH5 catalyzes the oxidative demethylation of N^6-methyladenine (m^6A) in single-stranded (ss) mRNA.[1] m^6A modifications play a critical role in regulating mRNA stability and metabolism, thereby influencing gene expression and affecting key cellular processes such as proliferation,[2] metastasis,[3] invasion,[4] and ossification.[5] Dysregulation of ALKBH5 has been implicated in the development and progression of various cancers.[6,7]

ALKBH5 belongs to the alkylation repair homolog B (AlkB) family of non-heme Fe(II)/2-oxoglutarate (2OG)-dependent oxygenases,[8,9] which includes bacterial AlkB enzyme[9,10] and nine human homologs: ALKBH1–8 and fat mass and obesity-associated protein (FTO; also known as ALKBH9).[9,11] Among these, only ALKBH5 and FTO function as RNA demethylases that modify m^6A.[1,12,13] FTO catalyzes the oxidative demethylation of m^6A via hydroxylation to form a hemiaminal intermediate (hm^6A; hydroxymethyladenine), whereas ALKBH5 directly removes the methyl group to yield adenine and formaldehyde.[14]

Non-heme Fe(II)/2OG-dependent oxygenases possess a characteristic distorted double-stranded β-helix (DSBH) core fold that harbors the Fe(II) center and its coordinated ligands.[8,15,16] The crystallographic structure of ALKBH5 in complex with ssRNA (PDB ID: 7WKV)[17,18] (Figure 1A) reveals distinctive structural features, including an extended βIV-V loop (residues 229–242) and a relatively long N-terminal extension with respect to other AlkB members. ALKBH5 also contains two nucleotide recognition lids (NRLs): NRL1 (residues 124–137) and NRL2 (residues 138–161), characteristic of the AlkB family,[10] located within the N-terminal region. In the crystal structure of ALKBH5, the active site Mn(II) ion (substituting for Fe(II) ion) is coordinated in a monodentate manner by two histidine residues (His204 and His266) and one aspartate residue (Asp206), together forming the canonical 2-His-1-carboxylate facial triad, a characteristic of many non-heme Fe(II)/2OG-dependent oxygenases. In addition to these facial triad residues, the co-substrate 2OG also coordinates with Mn(II) in a bidentate manner. The C1 carboxylate of 2OG coordinates Fe(II) in an *off-line* binding mode[19] as observed in other Fe(II)/2OG-dependent nucleic acids demethylases such as FTO,[20] AlkB,[21,22] and ALKBH2.[23] In this *off-line* mode, the C1 carboxylate binds *trans* to the His_2 (His266), in contrast to the *in-line* mode, where is coordinates *trans* to His_1 (His204). The active site is illustrated by the Fe(IV)=O intermediate (modeled as explained in the system setup in the computational methods section), as shown in Figure 1B. The substrate is an ssRNA tetramer containing m^6A, which binds in the active site and is stabilized by several key interactions. The 5′-phosphate group forms a salt bridge with the side chain of Arg130 from the NRL1 lid, while 2′-hydroxyl group of m^6A ribose interacts with the backbone carbonyl of Ser203 (Figure 2).[18] The purine ring of m^6A is oriented to engage in a π-π stacking interaction with the imidazole ring of the Fe(II)-coordinated His204, and its N^6 atom forms a hydrogen bond with the hydroxyl group of Tyr139.[18] Additionally, the purine ring of the guanine at the −1 position (G-1) forms a π-π interaction with the phenyl ring of Phe234 in the βIV-V loop.[18] These interactions collectively stabilize and maintain a catalytically productive orientation of the ssRNA substrate in the active site. However, the βIV-V loop in ALKBH5[24] is similar to the L1 loop in FTO,[25] which hinders the productive binding of dsDNA or RNA, thereby explaining the preference of both enzymes for ssRNA substrates. In addition, the high homology of the zebrafish and murine ALKBH5 can provide a good background for further validating computational models and for evolutionary studies.[26,27]

ALKBH5 follows the general mechanistic strategy of non-heme Fe(II)/2OG-dependent oxygenases,[8,15,16,28–31] as established by both experimental[15,16,29,30,32–37] and computational studies (Scheme 1).[38–49] In the resting state, the Fe(II) ion is coordinated to two histidine residues (His204, His266), one aspartate (Asp206), and three water molecules. Upon bidentate coordination of 2OG, two water molecules are displaced. The primary substrate then binds near the Fe(II) center, displacing the third water molecule and generating an open coordination site for O_2. A recent NMR study demonstrates that binding of the primary substrate, m^6A, to ALKBH5 induces a conformational shift of 2OG from an *off-line* to an *in-line* binding mode. This rearrangement is essential for exposing the metal center, thereby enabling the coordination of molecular oxygen (O_2).[50,51] Upon O_2 binding, a ferric-superoxo (Fe(III)–O–$O^{\cdot-}$) complex is formed. The distal oxygen (O_d) of Fe(III)–O–$O^{\cdot-}$ of this complex then performs a nucleophilic attack on the α--carbonyl

carbon (C2) of 2OG, resulting in the decarboxylation and formation of a Fe(II)-succinyl-peroxo intermediate.[52–57] Heterolytic cleavage of the O–O bond subsequently generates a catalytically reactive Fe(IV)=O (ferryl) species,[58–61] which is capable of oxidizing C–H bonds in the methyl group of the substrate.[39,62–66] Substrate C–H bond oxidation begins with hydrogen atom transfer (HAT) from m^6A by the ferryl species, generating a ferric hydroxo (Fe(III)–OH) complex and a substrate-based methylene radical. Rebound hydroxylation then occurs, resulting in the formation of hemiaminal (hm^6A) intermediate.

In contrast to FTO, where the reaction of the hemiaminal product to form formaldehyde and unmodified base occurs slowly and non-enzymatically,[14] ALKBH5 performs enzymatic fragmentation[67] of hm^6A, giving formaldehyde and adenine. Two mechanisms have been proposed for the ALKBH5-catalyzed hm^6A fragmentation based on structural and mutagenesis data.[18,67]

The first proposed mechanism (mechanism 1; Scheme 2)[18] involves a series of proton transfers with the participation of second coordination sphere (SCS) residues, Lys132 and Tyr139; it starts with an abstraction of a proton by Lys132 from the side chain hydroxyl group of Tyr139, followed by Tyr139 abstracting a proton from the hydroxyl group of hm^6A. Subsequently, formaldehyde is released, and adenine abstracts a proton from Lys132 (Scheme 2).[18]

An alternative mechanism (mechanism 2) proposed outlines two possible pathways that both begin with the formation of a nascent Schiff base.[67] In this mechanism, Lys132 serves as a proton donor, facilitating the release of a water molecule from hm^6A to form a Schiff base. The Schiff base can then either react with deprotonated Lys132 (pathway 1) or by Tyr139 (pathway 2), forming a protein-substrate intermediate. This is followed by the release of adenine and either a formation of an iminium ion (pathway 1) or an oxocarbenium intermediate (pathway 2) and subsequent release of formaldehyde (Scheme 3).

Previous mutagenesis studies of two key SCS residues in ALKBH5—Lys132 and Tyr139—further support their participation in the post-hydroxylation mechanism.[67] In particular, the K132Q variant exhibits reduced activity, giving hm^6A as a major product, similar to FTO[14]; and K132R and Y139A variants are catalytically inactive.[18]

Although the general catalytic mechanisms of non-heme Fe (II)/2OG-dependent oxygenases, have been investigated through both experimental[15,16,29,30,32–37] and computational studies,[38–49] a comprehensive understanding of the demethylation of m^6A in ssRNA by ALKBH5 remains elusive. Despite available experimental studies on the ALKBH5's structure,[18,27,68] mechanism,[18,67] mutants,[1,67,68] and inhibition,[69–74] significant knowledge gaps persist largely due to the previous absence of a crystal structure of the ALKBH5-ssRNA (m^6A) complex. Key aspects such as the geometric and electronic structures of the key transition states (TSs) and reaction intermediates (IMs), the role of SCS and long-range (LR) residues in catalysis, and how the enzyme's internal correlated motions correlate to its function have not been explored. Importantly, the chemical mechanism of the post-hydroxylation step remains unknown. These insights are crucial for efforts in enzyme redesign and the development of ALKBH5-specific inhibitors.

The recently elucidated crystal structure of the human ALKBH5-ssRNA (m^6A) complex (PDB ID: 7WKV)[17,18] provides a foundation to address these gaps by applying computational chemistry approaches. In this study, we leverage this structural information to investigate the complete catalytic mechanism of ALKBH5-mediated m^6A demethylation in ssRNA, applying molecular dynamics (MD)-based quantum mechanics/molecular mechanics (QM/MM) calculations.

RESULTS AND DISCUSSION

ALKBH5 dioxygen activation mechanism

To investigate dioxygen (O_2) activation in ALKBH5, we performed a 1 μs MD simulation of the reactive *in-line* ALKBH5-ssRNA-Fe(III)–O–$O^{\cdot-}$ complex (Figure S1). Root-mean-square deviation (RMSD), time-dependent profile of the distance between O_d and C2 of 2OG and root-mean-square fluctuations (RMSFs; Figures S2–S4) indicate a stable simulation with the distance between O_d and C2 of 2OG averaging at 4.24 Å (Figure S3). The βIV-V loop (residues 229–242) is characterized by high fluctuations (RMSF plot, Figure S4). The MD-generated ensemble of structures was subsequently used for QM/MM potential energy scans (PES) calculations. For O_2 activation, we used one snapshot, as we demonstrated in an earlier study, that O_2 activation is less sensitive to conformational changes of the RC.[48] O_2 activation begins with a nucleophilic attack by the O_d of Fe(III)–O–$O^{\cdot-}$ in RC1 on the C2 carbon of 2OG. This reaction leads to cleavage of the C1–C2 bond in 2OG and formation of an exothermic Fe(II)-peroxosuccinate intermediate (IM1), with a reaction energy of −48.1 kcal/mol (Figure 3A). The activation energy barrier for the nucleophilic attack is 9.1 kcal/mol, comparable to that observed in other Fe(II)/2OG enzymes such as FTO[48] (9.7 kcal/mol) and TET2[49] (9.1 kcal/mol), and slightly lower than that reported for ALKBH2 (*off-line*, 11.8 kcal/mol),[38] EFE (10.4 kcal/mol),[54] and BesD (17.7 kcal/mol).[57] Following the formation of the Fe(II)-peroxosuccinate intermediate (IM1), cleavage of the O_p–O_d bond occurs, leading to the formation of a Fe (III) partial bond intermediate (IM2) with an activation energy of 2.5 kcal/mol at the B3 level. This value is slightly higher than that reported for FTO[48] (0.5 kcal/mol) and ALKBH2[38] (*off-line*, 0.9 kcal/mol) but lower than that for TET2[49] (4.4 kcal/mol). IM2 is characterized by a partial O_p–O_d bond distance of 2.24 Å and a Fe–O_p bond distance of 1.78 Å (Figure 3B). IM2 subsequently rearranges to form a catalytically active *in-line* ferryl (Fe (IV)=O) complex, IM3, in which the Fe–O_p distance shortens to 1.62 Å and the O_p–O_d bond extends to 2.94 Å. The large energy drop (72.1 kcal/mol) associated with IM3 species in ALKBH5 is consistent with calculated reaction energies for the ferryl formation in other Fe(II)/2OG enzymes, such as TauD, as reported by Neese (−61.8 kcal/mol),[75] TET2 (−62.5 kcal/mol),[49] EFE (−50.9 kcal/mol),[76] and PHF8 (−68.8 kcal/mol).[19] Key geometric parameters of the O_2 activation stationary points are compared in Figure 3B. These calculations suggest that while the O_2 activation mechanism in ALKBH5 shares similarities with other non-heme Fe(II)/2OG-dependent enzymes, subtle structural differences likely contribute to ALKBH5's unique substrate specificity and catalytic efficiency.

Conformational dynamics of the reactant complex for the substrate oxidation (ALKBH5-ssRNA (m^6A) ferryl complex)

Studies on several non-heme Fe(II)/2OG-dependent oxygenases have shown that conformational dynamics influence the mutual orientation between the ferryl species and the substrate, thereby affecting HAT reactivity.[45,77,78] To explore the effects of conformational dynamics on the *in-line* ferryl complex with ssRNA, we performed a 1 μs MD simulation. The RMSD, time-dependent distance profile between the ferryl oxygen (O_p) and the methyl carbon (C) of m^6A, Fe–O_p–C angle plot, and RMSF data are presented in Figures S5–S9. In the RMSF plot (Figure S8), the fluctuations observed around 0–50 residues region are the N-terminal fluctuations, as confirmed by principal-component analysis (PCA; Figure 4B). The region, including 140–150 residues, corresponds to the highly flexible NRL2 segment (residues 138–161) of ALKBH5. The results indicate a stable complex, with an average RMSD of 1.75 Å (Figure S5). Key parameters relevant to HAT in ALKBH5 include the distance between the ferryl O_p and the methyl group C of the substrate (Figure S9), with an average value of 4.14 Å, and the Fe–O_p–C angle (average value 133°, Figure S7). These values, obtained from the MD simulation, indicate favorable proximity and orientation of the m^6A substrate for efficient HAT in ALKBH5. MD simulations of the ferryl complex reveal that an extensive network of interactions within the protein environment stabilizes the position of the m^6A substrate. These include stacking interactions involving the side chains of Tyr141 and Tyr139 in the NRL2 loop, as well as π-π interaction with the imidazole ring of His204, consistent with the crystal structure.[18] Additionally, m^6A forms a strong hydrogen bond between its N^3 atom and the hydroxyl group of Tyr139. The electrostatic interaction between the 5′-phosphate group of m^6A and the positively charged side chain of Arg130 from the NRL1 remains consistent throughout the MD simulation (Figure S10 and 95%). Furthermore, m^6A maintains a hydrogen-bonding network with Arg283, Arg130, Lys132, and the ferryl oxygen (O_p), consistent with the crystal structure.[18] The face of G-1 (guanine at the −1 position of the ssRNA strand) remains engaged in π-π interaction with the phenyl ring of Phe234 in the βIV-V loop, helping to anchor the RNA strand within the enzyme's active site throughout the MD simulation. Additionally, the backbone amide (NH) of Lys235 in the βIV-V loop formed a strong interaction (69%) with the 5′-hydroxyl oxygen of the guanine at −2 position (G-2) ribose sugar ring in ssRNA (Figure S11), further stabilizing the substrate. The N4 and the N4-amine hydrogens of C+1 (cytosine at the +1 position) form hydrogen bonds with the backbone amide hydrogen (NH) (Figure S12) and carbonyl oxygen of Val205 (Figure S13), respectively, contributing to the overall stabilization of the ssRNA strand in the active site. To further evaluate the strength of the hydrogen bond interactions, we calculated the lifetime of the hydrogen bonds in individual frames for interactions involving the phosphate and hydroxyl group of the guanine with the SCS residues Arg130 and Lys235, respectively (Figures S10 and S11). Our analysis reveals that the average lifetime of the hydrogen bond between the 5′-phosphate group of m^6A and Arg130 is 0.95 (lifetime range from 0 to 1, where 0 indicates no hydrogen bond interaction and 1 indicates a strong hydrogen bond, as shown in Figure S10). Similarly, the hydrogen bond between Lys235 and the 5′-hydroxyl oxygen of the guanine at the −2 position has an average lifetime of 0.80 (Figure S11). Notably, the ssRNA tetramer containing m^6A maintains the orientation observed in the X-ray structure,[18] while the conformational dynamics finely tune the SCS interactions to support productive catalysis.

Further, the Fe center of the ALKBH5 is rigid, which is in agreement with MD studies of other Fe(II)/2OG enzymes[38,48] (more information is provided in section S1).

Correlated motions in enzymes provide insights into how distant regions of the protein can influence catalysis.[79–83] These motions involve dynamic couplings between spatially separated parts of the system. We focus on correlated motions involving SCS residues that orient and stabilize the substrate and may modulate the reactivity at the Fe center. Notably, we investigate correlated motions of SCS residues that are energetically involved in the stabilization of TSs. Dynamic cross-correlation analysis (DCCA) of ALKBH5 reveals that the DSBH (residues 189–283) β-sheets (see secondary structures in Figure S14) positively correlate with each other, highlighting the structural stability of the DSBH fold (Figure 4A in blue boxes). Furthermore, the ssRNA substrate strand correlates with Fe-coordinated residues His204 and Asp206 in the βII strand of the DSBH, facilitating productive substrate orientation. The roles of NRL1 and the βIV-V loop in catalysis are highlighted by their positive correlations with the βII and βVII strands of the DSBH fold, suggesting their contribution to the overall compactness of the active site and productive substrate orientation. This has been further supported by experimental data showing a loss of ALKBH5 activity in NRL1 variants, R130A and K132A, as well as in the βIV-V loop double variant F232A/F234A.[18,68] NRL2 also exhibits positive correlation with the substrate strand, reinforcing its role in substrate recognition and catalysis, further supported by experimental evidence of a loss of ALKBH5 catalytic activity in NRL2 mutants Y139A and Y141A.[68] PCA (Figure 4B), illustrating the direction of motion and relative flexibility of different regions, reveals that the ALKBH5 Fe(IV)=O complex is relatively rigid, with the exception of its N-terminal region. PCA and DCCA suggest that although the reactant complex is relatively rigid, complex correlated motions may fine-tune catalysis and contribute to its effectiveness. Notably, the positive correlations of NRL1 and NRL2 with the ssRNA strand are unique for ALKBH5, not observed in either FTO[48] or ALKBH2,[38] potentially contributing to ALKBH5's distinct demethylation activity. Exploring these correlated motions advances our fundamental understanding of how LR dynamic networks of interactions can influence catalysis. In the long term, such knowledge can be used for enzyme redesign; by targeting remote interaction partners of catalytically relevant residues, it may be possible to modulate enzymatic activity in a precise and controlled manner without altering the active site directly.

Hydroxylation of m^6A in ALKBH5-ssRNA

In the first (HAT) step, the ferryl species abstracts a hydrogen atom from the methyl group of m^6A, generating a Fe(III)–OH intermediate and a substrate radical. In the second step (rebound hydroxylation), the hydroxyl group rebounds to the substrate radical, yielding the hm^6A intermediate.

Mechanism of HAT in the ALKBH5-ssRNA complex

The HAT mechanism was explored using five well-equilibrated structures from the MD simulations, where the RMSDs were very stable (Figure S5). We also considered key parameters relevant to catalysis, such as the distance between the O_p and the m^6A's C (Figure S6) and the Fe–O_p–C angle (Figure S7). Overall, the QM/MM calculations

for the HAT reaction were performed using multiple snapshots that closely resemble the average structure from the stable regions of the MD simulations. This approach allows for the estimation of the effects of the conformational variability of the RCs on the activation and reaction energies of the HAT reaction. Consistent with the previous studies,[52,64,65,84–88] the QM/MM calculations were carried out for the quintet state of the ALKBH5 Fe(IV)=O complex. The calculated energy barriers at the B3 level range from 18.2 to 22.0 kcal/mol (with a Boltzmann-weighted average of 19.0 kcal/mol; Figure 5A). These values are consistent with HAT mechanisms reported for other Fe(II)/2OG-dependent oxygenases,[41,45,47,89] including ALKBH2 (22.2 kcal/mol)[38] and FTO (20.2 kcal/mol).[48] The distance between the O_p and the substrate's C varies between 4.0 Å and 4.2 Å (Table S1), the Fe–O_p–C angle varies between 160.0 ° and 137.5° (Table S1) in these five snapshots, the activation barrier varies between 18.2 kcal/mol and 22.0 kcal/mol, and the reaction energy varies between −0.3 and −7.0 between kcal/mol, indicating a delicate dynamic influence on the geometric parameters that are of key importance for the HAT reaction (Figure 5). We acknowledge that this approach has certain limitations and that alternative QM/MM free energy methods could offer more comprehensive insights, for example, QM/MM metadynamics[90–92] or QM/MM potential of mean force.[93,94] However, such calculations are computationally intensive and subject to future work.

The calculated HAT reaction barrier for ALKBH5 (19.0 kcal/mol) is in good agreement with experimentally determined activation barriers reported for other Fe(II)/2OG enzymes. For comparison, experimentally derived rate-limiting activation barriers, derived using the Eyring equation, are 20.2 kcal/mol for FTO,[95] 21.1 kcal/mol for both TET2[96] and ALKBH1,[97] and 19.4 kcal/mol for AlkB.[98]

QM/MM optimized TSs from the five potential energy surfaces are shown in Figures 5B–5F, illustrating partial hydrogen transfer to the ferryl oxygen (O_p). In the lowest PES, the key distances observed in the RC2/IM3 intermediate are 1.62 Å for Fe–O_p, 3.64 Å for O_p–H, and 1.10 Å for C–H (Figure 6; Table S1). The calculated Fe(IV) spin density of 3.12 (Figure 6; Table S2) supports the +4-oxidation state. Additionally, the O_p spin density of 0.62 is consistent with experimental characterization of non-heme ferryl intermediates in the quintet spin state,[99] as well as with previous computational studies on other non-heme Fe(II)/2OG-dependent oxygenases.[38,100–102] Compared with RC2, the Fe–O_p and C–H distances in TS3 increased to 1.72 Å and 1.25 Å, respectively, while the O_p–H distance decreased to 1.35 Å, confirming partial HAT (Figure 6; Table S1). HAT results in the formation of the Fe(III)–OH intermediate (IM4), as indicated by the elongated Fe–O_p bond (1.83 Å) and the shortened O_p–H (0.98 Å) distances (Figure 6). The change in Fe spin density from 3.12 to 4.19 indicates an oxidation state change from +4 to +3. The formation of a radical on the substrate methyl carbon (C) is further confirmed by the change in the spin density to −0.81 (Table S2). The intermediate IM4 is exothermic (−1.0 kcal/mol at the B3 level) (Figure 5A). The lowest HAT activation energy barrier, 18.2 kcal/mol, is consistent with the barriers reported for FTO (19.4 kcal/mol)[48] and ALKBH2 (21.6 kcal/mol).[38] Notably, in both ALKBH5 and FTO,[48] the HAT reaction is exothermic, whereas in ALKBH2,[38] it is endothermic. HAT barriers for all five ALKBH5 reaction profiles are provided in Table S3. The QM/MM optimized geometries of the five HAT TSs and their superimposed structures are shown in Figures 5B–5G. The energies for all RC2 structures were set to zero for two

reasons: (1) after truncation of the MD snapshots for the QM/MM calculations (see methods section, QM/MM Calculations), each structure contained a different number of MM atoms, rendering their energies incomparable; and (2) this normalization enabled plotting all five HAT energy profiles on the same graph to illustrate differences in activation and reaction energies. HAT calculations performed by extending the QM region (including Arg283 and Tyr139) show consistent results with the standard model. More details are provided in section S2.

The analysis of the molecular orbital mechanism of HAT indicates σ-channel (more details are shown in section S3, Figures S25 and S26; Table S4).

Role of SCS residues in stabilizing HAT TS

To investigate the energetic contributions of SCS residues to the stabilization of the HAT TS (TS3), we performed EDA. EDA quantifies the difference in non-bonded interaction energies (coulombic and van der Waals) between individual residues in the MM region and the QM region of the optimized RC and TS structures (Figure 7). The EDA results indicate that SCS residues Val191 and Gln153 stabilize TS3 relative to RC2, with energy contributions of −1.4 kcal/mol and −1.3 kcal/mol, respectively. In contrast, SCS residues Lys132 and Arg283, as well as the LR residue Tyr133, destabilize TS3, contributing 1.3 kcal/mol, 2.6 kcal/mol, and 8.1 kcal/mol, respectively (Figures 7 and S15A). These interactions are largely consistent across the other four HAT TSs (TS3).

Mechanism of rebound hydroxylation in the ALKBH5-ssRNA complex

After HAT, the intermediate IM4 undergoes rebound hydroxylation via TS4, leading to the formation of the hm^{6}A intermediate (IM5). The Fe–O_p and O_p–C distances of 1.90 Å and 2.68 Å in TS4 indicate a partial transfer of the hydroxyl group from the Fe(III) center to the methyl carbon (Figure 6). In IM5, the C–O_p distance shortens to 1.42 Å, while the Fe–O_p bond elongates to 2.27 Å, accompanied by a spin density of 3.80 on Fe, consistent with a +2-oxidation state. The calculated activation energy barrier for rebound hydroxylation in ALKBH5 is 2.1 kcal/mol at the B3 level (Figure 8), substantially lower than the barriers reported for FTO[48] (9.2 kcal/mol) and ALKBH2 (6.1 kcal/mol),[38] indicating a relatively rapid rebound hydroxylation process in the ALKBH5-ssRNA complex. A reaction energy of −27.5 kcal/mol suggests that formation of the hm^{6}A intermediate is energetically favorable.

The EDA results suggest that TS4 is stabilized by the same SCS residues that stabilize the HAT TS3, specifically, Gln153 (−0.97 kcal/mol) and Val191 (−0.70 kcal/mol), while it is destabilized by SCS residues Arg283 (3.62 kcal/mol) and Lys132 (1.81 kcal/mol), as well as the LR residue Tyr133 (0.82 kcal/mol) compared with IM4 (Figure S15B).

Molecular orbital analysis provides valuable insights into the electronic structure and reaction mechanism; yet, it has been less explored for the rebound hydroxylation step in ALKBH5. To address this gap, we performed an SNO analysis of the rebound hydroxylation reaction (Figure S16). The analysis reveals that an electron from the ϕ_c orbital migrates into the π^*_{xz} anti-bonding orbital, triggering cleavage of the Fe–O_p bond. The bond cleavage facilitates the formation of new C–O_p σ--orbitals. The spin density on the carbon indicates

that a β--electron is transferred from the substrate radical to the antibonding orbital of the Fe(III)–OH group, in agreement with prior studies of non-heme Fe(II)/2OG-dependent JmjC oxygenases.[103,104]

Post-hydroxylation reactivity of ALKBH5: Conformational dynamics of the hm^{6}A intermediate

To explore the role of the conformational flexibility of the hm^{6}A intermediate in ALKBH5 catalysis, we performed a 1 μs MD simulation. The RMSD graph and the time-dependent profiles of key distances are provided in Figures S17 and S18. In the hm^{6}A intermediate, the N^6 atom and the phosphate oxygen are stabilized by strong hydrogen bonds with the hydroxyl group of Tyr139 and the backbone NH group of Val202, respectively. Additionally, the hydroxyl group of hm^{6}A forms strong hydrogen bonds with the non-coordinating oxygen of succinate and with Arg283.

DCCA analysis of the hm^{6}A intermediate (Figure 9A, black box) reveals that the NRL1 loop exhibits anti-correlated motions with the βIV-V loop and NRL2, indicating ALKBH5's preference for m^{6}A over the hm^{6}A substrate. PCA analysis (Figure 9B) further shows that the NRL1 loop, the βIV-V loop, and the substrate ssRNA strand move away from the active site, indicating that the hm^{6}A complex adopts a less compact conformation compared with the ferryl complex (Figure 4). In contrast to the ferryl, the highly flexible NRL2 loop shifts slightly away from the substrate strand. This increased flexibility may be associated with the final stages of catalysis and the enzyme's preparation for product release.

Post-hydroxylation of the hm^{6}A intermediate

The post-hydroxylation in ALKBH5 proceeds through fragmentation of hm^{6}A into adenine and formaldehyde via two distinct pathways: a series of proton transfers (mechanism 1, Scheme 2) or an alternative route involving Schiff base formation (mechanism 2, Scheme 3).

Decomposition of hm^{6}A via mechanism 1

Mechanism 1 requires deprotonated Lys132; therefore, we selected Asp125, located near Lys132, as the proton acceptor (Scheme S1). The studies indicate that the reaction involves a water-mediated proton transfer from Lys132 to Asp125 and occurs via TS5, with a barrier of 16.7 kcal/mol with respect to RC3/IM5 (Figure 8), resulting in IM6. In TS5, the Lys132–N–H and water–O–H bond distances elongate to 1.48 Å and 1.12 Å, respectively, consistent with a partial proton transfer from Lys132 to Asp125 through the bridging water molecule (Figures 10 and S19). Protonation of Asp125 is confirmed by the formation of an O–H bond (1.09 Å) and the elongation of the Lys132N—H distance to 1.54 Å in IM6.

We further performed MD simulations of IM6 since QM/MM calculations using IM6 structures optimized directly from the minimum energy reaction path were not productive, suggesting that conformational dynamics may contribute to the formation of catalytically productive IM6. Therefore, we performed MD simulations to obtain a favorable reactive conformation.

A stable trajectory of IM6 was observed (Figures S20 and S21), and subsequent QM/MM calculations were carried out with a snapshot selected by observing distances between the SCS residues (Lys132, Tyr139, and Asp125) and the substrate (hm^{6}A). The QM region includes side chains of Tyr139, Lys132, and Asp125, and three water molecules: two of them between Tyr139 and Lys132 and one between Lys132 and the substrate, hm^{6}A. To prepare the model, we adjusted the positions of the two water molecules bridging Tyr139 and Lys132 and refined the orientation of Tyr139, then optimized the MD snapshot to generate IM6' (Figures 10 and 11). The water molecules were included to facilitate the proton transfer, as the residues and the substrate (Lys132, Tyr139, and hm^{6}A) were not positioned closely enough to allow direct proton transfer.[105,106] Notably, a water molecule bridging Lys132 and Tyr139 is present in the crystallographic structure of the ALKBH5-ssRNA (m^{6}A) complex (PDB ID: 7WKV, Chain A).[17,18] In addition, water molecules in this region naturally emerged during the MD simulation. Their presence was consistently maintained throughout the 1 μs productive MD simulation. While we do not have direct experimental conformation, the crystallographic structure and the well-validated MD strongly support the plausible existence of water molecules bridging Lys132 and Tyr139. In the IM6′ complex, the post-hydroxylation reaction is initiated by proton transfer from Tyr139 to Lys132 via two water molecules (Water-1 and Water-2 in Figure 11), with an activation barrier of 24.2 kcal/mol at the B3 level. This step proceeds via TS6, characterized by Tyr139–O–H and Lys132–N–H distances of 1.31 Å and 1.05 Å, respectively, indicating partial dissociation of the Tyr139–O–H bond and formation of the Lys132–N–H bond. In the resulting IM7 intermediate, deprotonation of Tyr139 and protonation of Lys132 are confirmed by the elongated Tyr139–O–H distance (1.60 Å) and the shortened Lys132–N–H distance (1.05 Å). This step appears to represent the highest energy barrier in the post-hydroxylation process, although delicate/subtle conformational changes may further modulate its energy. In IM7, the deprotonated Tyr139 abstracts the hydroxyl proton from hm^{6}A, leading to the release of formaldehyde. During this fragmentation, the N^6 atom of adenine abstracts a proton from Lys132 via a water molecule (Water-3, Figure 11), completing the proton transfer cycle with an activation barrier of 20.8 kcal/mol at the B3 level (Figure 8). This step proceeds through TS7, characterized by slight elongation of Tyr139–O–H bond (1.03 Å), hm^{6}A–N^6–C bond (1.56 Å), and the Lys132–N–H (1.65 Å), along with shortening of the hm^{6}A–N^6–H distance to 1.38 Å compared with their respective distances in IM7. In IM8, the formation of formaldehyde is evidenced by the carbonyl bond distance (1.21 Å) and the elongated N^6–C distance in hm^{6}A (2.91 Å). The restored adenine is confirmed by the N^6–H bond length of 1.03 Å. In this state, deprotonated Lys132 abstracts a proton from Asp125 through a barrierless process, yielding the highly exothermic final product (PD), with a reaction energy of −62.0 kcal/mol relative to IM6' (Figure 8). The Lys132–N–H bond distance of 1.06 Å in PD indicates complete protonation of Lys132. Although this proton transfer is barrierless, Lys132 must adopt specific conformational changes to facilitate the transfer. The second proton transfer step (IM6′ to TS6) could be the highest energy barrier (24.2 kcal/mol) in both the post-hydroxylation process and the entire reaction, slightly exceeding the experimentally observed activation barrier for ALKBH5 demethylation of m^{6}A (20.9 kcal/mol).[1,24] The hydroxyl group of Tyr139 plays a critical role in the post-hydroxylation fragmentation of hm^{6}A, including the rate-limiting step. This is supported experimentally by a considerable decrease in reaction rate observed

in the Y139F variant and the complete loss of catalytic activity in the Y139A variant.[14] The involvement of Lys132 in the post-hydroxylation process is further supported by the reduced activity of the K132Q variant, which predominantly produces hm^{6}A as FTO,[67] and by the complete loss of catalytic activity in the K132R.[18] Moreover, the overall k_{cat} of ALKBH5[1,24] is in reasonable agreement with the predicted activation barrier of the rate-limiting step, corresponding to 20.9 kcal/mol calculated from the experimental rate constant using the Eyring equation and 24.2 kcal/mol as determined by QM/MM reaction paths calculations.

Decomposition of hm^{6}A via mechanism 2

An alternative proposal for hm^{6}A fragmentation involves the formation of a nascent Schiff base (mechanism 2; Scheme 3). In this mechanism, Lys132 acts as a proton donor, promoting the elimination of a water molecule from hm^{6}A and generating the Schiff base. The Schiff base can then react either with deprotonated Lys132 (pathway 1) or with Tyr139 (pathway 2), resulting in a protein-substrate adduct. Subsequent cleavage of this adduct yields adenine and forms either an iminium or an oxocarbenium ion intermediate, respectively. Hydrolysis of these intermediates ultimately releases formaldehyde (Scheme 3).

Despite extensive attempts, our calculations did not support the formation of a stable Schiff base intermediate due to the inherent instability (section S4). We also investigated an alternative mechanism in which Lys132 could form a protein-substrate adduct by performing a nucleophilic attack during the generation of a Schiff base-like structure through suprafacial displacement of a water molecule (Scheme S2). However, this pathway exhibited a prohibitively high activation barrier of 47.8 kcal/mol at the B3 level (TS_{ch1}; Figure 12), rendering it energetically unfeasible. We also evaluated an antarafacial displacement mechanism for water elimination to form a Lys132-protein-substrate intermediate (Scheme S2). To this end, we selected three different snapshots from the MD of the ALKBH5-hm^{6}A intermediate and performed the antarafacial displacement calculations. Unfortunately, two of these attempts yielded activation barriers comparable to those observed for the suprafacial displacement (43.4 kcal/mol and 56.4 kcal/mol), while the third resulted in an even higher barrier of 83.7 kcal/mol (Figure S23). These results are consistent with the energetically unfavorable profiles observed for the suprafacial displacements, which are represented in Figures 12 and S23. Additionally, we considered a mechanism in which Lys132 serves as a proton donor during hm^{6}A dehydration, followed by a nucleophilic attack by Tyr139 on the resulting Schiff base to generate a Tyr139-protein-substrate intermediate (Scheme S3). However, this route ultimately led back to the formation of a Lys132-protein-substrate adduct with a high barrier of 46.9 kcal/mol (Figure S24), making this mechanism similarly unlikely.

These findings indicate that neither the Schiff base formation (mechanism 2) nor alternative pathways involving protein-substrate intermediates are energetically favorable. Instead, mechanism 1[18] emerges as the most plausible pathway for the post-hydroxylation reaction.

Several studies have reported deformylation of substrates following hydroxylation.[79,107,108] For example, a computational study on FTO demonstrated a 23.1 kcal/mol energy barrier for

water-assisted deformylation of hm^{6}A in aqueous solution, consistent with the experimental value of approximately 24 kcal/mol.[109] In contrast, the same process within the enzyme environment showed a much higher barrier of 76.6 kcal/mol.[79] Similarly, a study of the catalytic mechanism of melatonin metabolism by CYP1A1 found that deformylation of hydroxylated melatonin occurs more effectively within the enzyme than through water-assisted pathways in solution.[108] A study on the CYP51 enzyme reported that the overall barrier for the deformylation mechanism within the enzyme is approximately 6.8 kcal/mol.[107] Our study further extends understanding of the post-hydroxylation mechanism within the specific arrangement of interactions in ALKBH5. While the hydroxylation of m^{6}A was investigated in FTO by Shaik[96] and by our group,[47] the unique catalytic mechanism of the m^{6}A-specific demethylase ALKBH5 has not been explored previously due to the absence of a crystal structure in complex with the substrate. The availability of the recent crystal structure of ALKBH5 bound to RNA containing m^{6}A (PDB ID: 7WKV)[17,18] enabled us to investigate its catalytic mechanism and the distinctive SCS interactions that differentiate ALKBH5 from FTO, thus shedding light on its substrate selectivity. Notably, experimental studies have shown that the post-hydroxylation steps occur within the enzyme, in contrast to enzymes such as FTO. Although several reaction mechanisms have been proposed for this transformation, their feasibility has not been critically assessed. In this study, we systematically explored three alternative experimentally derived mechanisms and, for the first time, identified the most probable pathway.

In this study, we employed computational methods to investigate the catalytic mechanism of ALKBH5 conversion of m^{6}A to adenine and formaldehyde.

While dioxygen activation in ALKBH5 shares common mechanistic features with other non-heme Fe(II)/2OG-dependent oxygenases, it is distinguished by unique energy barriers and structural characteristics that likely underline its high catalytic efficiency. The HAT step proceeds via a σ-channel electron transfer pathway with a Boltzmann-weighted average barrier of 19.0 kcal/mol, comparable to that in FTO (20.2 kcal/mol) and ALKBH2 (22.2 kcal/mol). Notably, the rebound hydroxylation barrier in ALKBH5 (2.1 kcal/mol) is significantly lower than that in FTO (9.2 kcal/mol) and ALKBH2 (6.1 kcal/mol), reinforcing its catalytic efficiency.

Our QM/MM calculations evaluated two proposed mechanisms for the post-hydroxylation fragmentation of the hm^{6}A intermediate: mechanism 1, involving proton transfers mediated by SCS residues, and mechanism 2, including Schiff base formation. The results support mechanism 1 as the most probable, with a series of proton transfers facilitated by Tyr139, Lys132, and Asp125. Among these, the proton transfer from Tyr139 to Lys132 was identified as the rate-limiting step, exhibiting a barrier of 24.2 kcal/mol, consistent with the experimentally reported activation barrier for ALKBH5 demethylation. Previous experimental studies have highlighted the role of the SCS residues Lys132 and Tyr139 in the catalytic mechanism of ALKBH5.[18,67] Consistent with these findings, our calculations also demonstrate that these residues are crucial for the reactions catalyzed by ALKBH5, particularly in the post-hydroxylation mechanism involving proton transfer. In contrast, mechanism 2, whether proceeding via classical Schiff base formation or alternative routes, was found to be energetically unfavorable.

While both ALKBH5 and FTO initiate substrate hydroxylation via comparable hydrogen atom transfer (HAT) barriers and mechanism (follow a σ-channel electron transfer pathway), only ALKBH5 catalyzes complete conversion to adenine and formaldehyde; FTO, in contrast, produces a stable hydroxymethyl intermediate (hm^{6}A), with slow, non-enzymatic fragmentation. Our study elucidates key mechanistic distinctions between the two enzymes, highlighting ALKBH5's lower rebound hydroxylation barrier and identifying SCS residues, Lys132 and Tyr139, as critical to its catalytic mechanism, in agreement with experimental observations. Additionally, Val191 and Tyr133 were found to contribute specifically to ALKBH5 function, differentiating it from other ALKBH family members. We further demonstrate that conformational dynamics and allosteric networks in ALKBH5 play a central role in catalysis. Correlated motions between NRL1, NRL2, and the βIV-V loop, as well as their interactions with ssRNA, appear to support catalytic demethylation. Notably, enhanced flexibility of the NRL2 loop in the hm^{6}A intermediate, compared with the ferryl state, may facilitate key proton transfer steps during post-hydroxylation fragmentation. Altogether, these findings offer a comprehensive mechanistic understanding of ALKBH5 function and its unique catalytic strategy. This knowledge provides a valuable framework for the rational redesign of ALKBH5 and the development of selective inhibitors targeting RNA methylation pathways for therapeutic applications.

METHODS

Computational methods

An X-ray crystal structure of the complex between ALKBH5 and ssRNA containing m^{6}A (PDB ID: 7KWV)[17,18] was used as the starting point for modeling. In the crystal structure, the active site contains catalytically inert Mn(II) coordinated by 2OG in a bidentate manner and in *off-line* mode, two histidines (His204 and His266) in monodentate fashion, a monodentate aspartate (Asp206), and a water molecule. The Mn(II) was replaced with the catalytically active Fe(II), and the binding mode of 2OG was converted to a productive *in-line* orientation[50] (Figure 13) using Gauss View 6.0.[110] The protonation states of ionizable groups were assigned using PROPKA.[111] The protonation and tautomeric states of the histidine residues coordinating the Fe(II) center were verified by visual inspection in UCSF Chimera.[112] To generate parameters for the Fe(III)–O–O$^{\cdot-}$ intermediate, an O_2 molecule replaced the metal-coordinated water in an end-on fashion (Figure 13). Parameters for the non-standard molecules, 2OG, m^{6}A, and O_2, were generated using the Antechamber module in Amber18.[113] The Metal Center Parameter Builder (MCPB.py)[114] in Amber18 was used to generate parameters for the active site Fe(III) (high spin S = 2, M = 5) and its coordinating ligands. Bond and angle force constants were derived using the Seminario method,[115] and partial charges were calculated with the RESP charge fitting (ChgModB) method.[116] The remaining protein residues were parametrized using the Amber FF14SB[117] force field. The t-leap module of Amber18 was used to neutralize the system by adding Na^+ counterions. The system was solvated using the Transferable Intermolecular Potential 3-Point (TIP3P) water model[118] in a rectangular box extending at least 10 Å from the protein surface. The ferryl complex and hemiaminal intermediate were prepared by replacing 2OG with monodentate succinate, O_2 with O^{2-}, and m^{6}A with hm^{6}A, respectively. The MD setups of the different systems, ALKBH5-Fe(III)-superoxide-ssRNA(m^{6}A), ALKBH5-Fe(IV)=O-

ssRNA(m^6A), ALKBH5-Fe(II)-ssRNA(hm^6A), and ALKBH5-IM6, contained a total of: 32,042, 32,030, 32,040, and 32,042 atoms, respectively (3,692, 3,689, 3,689, and 3,689 protein atoms and 9,448, 9,445, 9,449, and 9,449 water molecules, respectively). The RNA was modeled using the AMBER18-FF14SB force field.

MD simulations

Two energy minimizations were performed before initiating the MD simulations. In the first minimization, only the water molecules and Na^+ counterions were minimized while restraining the enzyme with a harmonic potential of 500 kcal mol^{-1} $Å^{-2}$. In the second minimization, the entire system was optimized without restraints. For both minimizations, the first 5000 steps used the steepest descent algorithm, followed by 5000 steps of conjugate gradient minimization. The system was then gradually heated over 100 ps. During the first 50 ps, the temperature increased from 0 K to 300 K; during the remaining 50 ps, the temperature was maintained at 300 K, using a Langevin thermostat[119] under constant volume (NVT ensemble) conditions. The solute was restrained with a harmonic potential of 50 kcal mol^{-1} $Å^{-2}$ during heating. To achieve uniform density, a weak harmonic restraint of 5 kcal mol^{-1} $Å^{-2}$ was applied for 1 ns using an NPT canonical ensemble. The system was then equilibrated (initial equilibration) within the NPT ensemble at constant temperature and pressure (300 K and 1 bar) for 3 ns without restraints. Production dynamics were conducted for 1 μs under the NPT ensemble. Pressure control was achieved using a Berendsen barostat,[120] and the SHAKE algorithm[121] was used to constrain bond vibrations involving hydrogen atoms. LR electrostatic interactions were treated with the particle mesh Ewald (PME) method,[122] using a cutoff distance of 10 Å. The MD simulations were performed using the GPU-enabled PMEMD module of the Amber18. Periodic boundary conditions were applied throughout all simulations. No constraints were applied to the RNA substrate or any other part of the system during the MD simulations. MD trajectory analysis, including RMSD, RMSF, hydrogen bonding analysis, and electrostatic analysis, was conducted using the CPPTRAJ module of Amber18.[123] DCCA and PCA were performed using the Bio3D module in the R package.[124]

QM/MM calculations

Chemshell[125] was used to perform the QM/MM calculations. Turbomole[126] was employed for the QM region, and DL_POLY[127] for the MM region. For dioxygen activation, the QM/MM system contained 62 QM atoms (Figure 13) and 17,193 MM atoms, with four link atoms[128] used to treat the covalent bonds at the QM/MM boundary. For HAT and rebound hydroxylation reactions, the QM region contained 59 QM and 17,355 MM atoms, and four link atoms. Several extended QM regions were also examined for HAT: with Arg283 included, the QM region contained 77 atoms and 17,337 MM atoms, and five link atoms; with Tyr139 included, the QM region contained 74 atoms and 17,340 MM atoms, with five link atoms; and including both Arg283 and Tyr139, the QM region contained 92 atoms and 17,322 MM atoms, with six link atoms. For the proton transfer-mediated post-hydroxylation mechanism (mechanism 1), the QM region for the first step contained 99 QM atoms and 17,315 MM atoms, with seven link atoms. For the second step and subsequent steps, the system contained 99 QM atoms and 16,940 MM atoms, with seven link atoms. For the alternative pathways leading to the Schiff base formation mechanism, the system

comprised 90 QM atoms and 17,687 MM atoms, also with seven link atoms. In all systems, atoms within 8 Å of the QM region were allowed to move during minimization. All water molecules beyond 12 Å from the protein surface were removed. The interaction between the QM and MM regions was described using the electronic embedding method. The MM region was modeled with the Amber FF14SB force field, while the QM region was treated with the unrestricted B3LYP (UB3LYP) functional. Geometry optimizations were performed using the def2-SVP basis set (B1) for all atoms. Starting from the optimized reactant complex (RC), PES along the reaction coordinate was conducted in small increments (0.1 Å) to locate TSs and IMs using a DL-find optimizer.[129] The TS geometries were then optimized without restraints using the dimer method[130] in Chemshell. Single-point energy calculations were performed, with the higher basis set def2-TZVP (B2) for all atoms to improve the energies of the optimized stationary points. Frequency calculations were performed to confirm that the stationary points correspond to TSs or minima. Zero-point energy (ZPE) obtained from these frequency calculations was added to the B2 energies to yield the final B3 (B2+ZPE) energies. Molecular orbitals were analyzed using spin natural orbital (SNO) analysis.[131] Energy decomposition analysis (EDA) was performed using the Fortran90 program developed by Cisneros et al.[132]

RESOURCE AVAILABILITY

Lead contact

Request for further information and resources will be fulfilled by the lead contact, Tatyana G. Karabencheva-Christova (tatyanak@mtu.edu).

Materials availability

The study did not use or generate any materials.

Data and code availability

The data that support the plots within this paper will be available from the lead contact upon request.

Supplementary Material

Refer to Web version on PubMed Central for supplementary material.

ACKNOWLEDGMENTS

Research reported in this publication was supported by the National Institute of General Medical Sciences of the National Institutes of Health, United States, under award no. R35GM156437.

REFERENCES

1. Zheng G, Dahl JA, Niu Y, Fedorcsak P, Huang C-M, Li CJ, Vågbø CB, Shi Y, Wang W-L, Song S-H, et al. (2013). ALKBH5 is a mammalian RNA demethylase that impacts RNA metabolism and mouse fertility. Mol. Cell 49, 18–29. 10.1016/j.molcel.2012.10.015. [PubMed: 23177736]
2. Chao Y, Shang J, and Ji W (2020). ALKBH5-m6A-FOXM1 signaling axis promotes proliferation and invasion of lung adenocarcinoma cells under intermittent hypoxia. Biochem. Biophys. Res. Commun. 521, 499–506. 10.1016/j.bbrc.2019.10.145. [PubMed: 31677788]

3. Jin D, Guo J, Wu Y, Yang L, Wang X, Du J, Dai J, Chen W, Gong K, Miao S, et al. (2020). m6A demethylase ALKBH5 inhibits tumor growth and metastasis by reducing YTHDFs-mediated YAP expression and inhibiting miR-107/LATS2-mediated YAP activity in NSCLC. Mol. Cancer 19, 40. 10.1186/s12943-020-01161-1. [PubMed: 32106857]
4. Li X-C, Jin F, Wang B-Y, Yin X-J, Hong W, and Tian F-J (2019). The m6A demethylase ALKBH5 controls trophoblast invasion at the maternal-fetal interface by regulating the stability of CYR61 mRNA. Theranostics 9, 3853–3865. 10.7150/thno.31868. [PubMed: 31281518]
5. Wang H-F, Kuang M-J, Han S-J, Wang A-B, Qiu J, Wang F, Tan B-Y, and Wang D-C (2020). BMP2 Modified by the m6A Demethylation Enzyme ALKBH5 in the Ossification of the Ligamentum Flavum Through the AKT Signaling Pathway. Calcif. Tissue Int. 106, 486–493. 10.1007/s00223-019-00654-6. [PubMed: 31897529]
6. Zhou Z, Lv J, Yu H, Han J, Yang X, Feng D, Wu Q, Yuan B, Lu Q, and Yang H (2020). Mechanism of RNA modification N6-methyladenosine in human cancer. Mol. Cancer 19, 104. 10.1186/s12943-020-01216-3. [PubMed: 32513173]
7. Gu C, Shi X, Dai C, Shen F, Rocco G, Chen J, Huang Z, Chen C, He C, Huang T, and Chen C (2020). RNA m6A Modification in Cancers: Molecular Mechanisms and Potential Clinical Applications. Innovation 1, 100066. 10.1016/j.xinn.2020.100066. [PubMed: 34557726]
8. Hausinger RP (2004). FeII/alpha-ketoglutarate-dependent hydroxylases and related enzymes. Crit. Rev. Biochem. Mol. Biol. 39, 21–68. 10.1080/10409230490440541. [PubMed: 15121720]
9. Zheng G, Fu Y, and He C (2014). Nucleic Acid Oxidation in DNA Damage Repair and Epigenetics. Chem. Rev. 114, 4602–4620. 10.1021/cr400432d. [PubMed: 24580634]
10. Fedeles BI, Singh V, Delaney JC, Li D, and Essigmann JM (2015). The AlkB Family of Fe(II)/α-Ketoglutarate-dependent Dioxygenases: Repairing Nucleic Acid Alkylation Damage and Beyond. J. Biol. Chem. 290, 20734–20742. 10.1074/jbc.R115.656462. [PubMed: 26152727]
11. Gerken T, Girard CA, Tung Y-CL, Webby CJ, Saudek V, Hewitson KS, Yeo GSH, McDonough MA, Cunliffe S, McNeill LA, et al. (2007). The obesity-associated FTO gene encodes a 2-oxoglutarate-dependent nucleic acid demethylase. Science 318, 1469–1472. 10.1126/science.1151710. [PubMed: 17991826]
12. Jia G, Fu Y, Zhao X, Dai Q, Zheng G, Yang Y, Yi C, Lindahl T, Pan T, Yang Y-G, and He C (2011). N6-Methyladenosine in nuclear RNA is a major substrate of the obesity-associated FTO. Nat. Chem. Biol. 7, 885–887. 10.1038/nchembio.687. [PubMed: 22002720]
13. Shen D, Wang B, Gao Y, Zhao L, Bi Y, Zhang J, Wang N, Kang H, Pang J, Liu Y, et al. (2022). Detailed resume of RNA m6A demethylases. Acta Pharm. Sin. B 12, 2193–2205. 10.1016/j.apsb.2022.01.003. [PubMed: 35646549]
14. Shishodia S, Zhang D, El-Sagheer AH, Brown T, Claridge TDW, Schofield CJ, and Hopkinson RJ (2018). NMR analyses on N-hydroxymethylated nucleobases – implications for formaldehyde toxicity and nucleic acid demethylases. Org. Biomol. Chem. 16, 4021–4032. 10.1039/C8OB00734A. [PubMed: 29767200]
15. Schofield CJ, and Zhang Z (1999). Structural and mechanistic studies on 2-oxoglutarate-dependent oxygenases and related enzymes. Curr. Opin. Struct. Biol. 9, 722–731. 10.1016/S0959-440X(99)00036-6. [PubMed: 10607676]
16. Allpress CJ, Kleespies ST, and Que L (2015). Synthetic models of 2-oxoglutarate-dependent oxygenases. In 2-Oxoglutarate-Dependent Oxygenases RSC Metallobiology, Hausinger RP and Schofield CJ, eds. (Royal Society of Chemistry), pp. 123–148. 10.1039/9781782621959-00123.
17. Berman HM, Westbrook J, Feng Z, Gilliland G, Bhat TN, Weissig H, Shindyalov IN, and Bourne PE (2000). The Protein Data Bank. Nucleic Acids Res. 28, 235–242. 10.1093/nar/28.1.235. [PubMed: 10592235]
18. Kaur S, Tam NY, McDonough MA, Schofield CJ, and Aik WS (2022). Mechanisms of substrate recognition and N6-methyladenosine demethylation revealed by crystal structures of ALKBH5-RNA complexes. Nucleic Acids Res. 50, 4148–4160. 10.1093/nar/gkac195. [PubMed: 35333330]
19. Chaturvedi SS, Ramanan R, Lehnert N, Schofield CJ, Karabencheva-Christova TG, and Christov CZ (2020). Catalysis by the Non-Heme Iron(II) Histone Demethylase PHF8 Involves Iron Center Rearrangement and Conformational Modulation of Substrate Orientation. ACS Catal. 10, 1195–1209. 10.1021/acscatal.9b04907. [PubMed: 31976154]

20. Han Z, Niu T, Chang J, Lei X, Zhao M, Wang Q, Cheng W, Wang J, Feng Y, and Chai J (2010). Crystal structure of the FTO protein reveals basis for its substrate specificity. Nature 464, 1205–1209. 10.1038/nature08921. [PubMed: 20376003]
21. Yu B, and Hunt JF (2009). Enzymological and structural studies of the mechanism of promiscuous substrate recognition by the oxidative DNA repair enzyme AlkB. Proc. Natl. Acad. Sci. 106, 14315–14320. 10.1073/pnas.0812938106. [PubMed: 19706517]
22. Yi C, Jia G, Hou G, Dai Q, Zhang W, Zheng G, Jian X, Yang C-G, Cui Q, and He C (2010). Iron-catalysed oxidation intermediates captured in a DNA repair dioxygenase. Nature 468, 330–333. 10.1038/nature09497. [PubMed: 21068844]
23. Yi C, Chen B, Qi B, Zhang W, Jia G, Zhang L, Li CJ, Dinner AR, Yang C-G, and He C (2012). Duplex interrogation by a direct DNA repair protein in search of base damage. Nat. Struct. Mol. Biol. 19, 671–676. 10.1038/nsmb.2320. [PubMed: 22659876]
24. Aik W, Scotti JS, Choi H, Gong L, Demetriades M, Schofield CJ, and McDonough MA (2014). Structure of human RNA N^6-methyladenine demethylase ALKBH5 provides insights into its mechanisms of nucleic acid recognition and demethylation. Nucleic Acids Res. 42, 4741–4754. 10.1093/nar/gku085. [PubMed: 24489119]
25. Han Z, Huang N, Niu T, and Chai J (2010). A loop matters for FTO substrate selection. Protein Cell 1, 616–620. 10.1007/s13238-010-0082-2. [PubMed: 21203933]
26. Tang C, Klukovich R, Peng H, Wang Z, Yu T, Zhang Y, Zheng H, Klungland A, and Yan W (2018). ALKBH5-dependent m6A demethylation controls splicing and stability of long 3'-UTR mRNAs in male germ cells. Proc. Natl. Acad. Sci. USA 115, E325–E333. 10.1073/pnas.1717794115. [PubMed: 29279410]
27. Chen W, Zhang L, Zheng G, Fu Y, Ji Q, Liu F, Chen H, and He C (2014). Crystal structure of the RNA demethylase ALKBH5 from zebrafish. FEBS Lett. 588, 892–898. 10.1016/j.febslet.2014.02.021. [PubMed: 24561204]
28. Islam MS, Leissing TM, Chowdhury R, Hopkinson RJ, and Schofield CJ (2018). 2-Oxoglutarate-Dependent Oxygenases. Annu. Rev. Biochem. 87, 585–620. 10.1146/annurev-biochem-061516-044724. [PubMed: 29494239]
29. Martinez S, and Hausinger RP (2015). Catalytic Mechanisms of Fe(II)- and 2-Oxoglutarate-dependent Oxygenases. J. Biol. Chem. 290, 20702–20711. 10.1074/jbc.R115.648691. [PubMed: 26152721]
30. Solomon EI, DeWeese DE, and Babicz JT Jr. (2021). Mechanisms of O2 Activation by Mononuclear Non-Heme Iron Enzymes. Biochemistry 60, 3497–3506. 10.1021/acs.biochem.1c00370. [PubMed: 34266238]
31. Bruijnincx PCA, van Koten G, and Klein Gebbink RJM (2008). Mononuclear non-heme iron enzymes with the 2-His-1-carboxylate facial triad: recent developments in enzymology and modeling studies. Chem. Soc. Rev. 37, 2716–2744. 10.1039/B707179P. [PubMed: 19020684]
32. Shi M, and Shen L (2017). The Molecular Basis of DNA Demethylation. In DNA and Histone Methylation as Cancer Targets, Kaneda A and Tsukada Y, eds. (Springer International Publishing), pp. 53–73. 10.1007/978-3-319-59786-7_3.
33. Jacobs AB, Banerjee R, Deweese DE, Braun A, Babicz JT Jr., Gee LB, Sutherlin KD, Böttger LH, Yoda Y, Saito M, et al. (2021). Nuclear Resonance Vibrational Spectroscopic Definition of the Fe(IV)2 Intermediate Q in Methane Monooxygenase and Its Reactivity. J. Am. Chem. Soc. 143, 16007–16029. 10.1021/jacs.1c05436. [PubMed: 34570980]
34. Srnec M, Wong SD, Matthews ML, Krebs C, Bollinger JM Jr., and Solomon EI (2016). Electronic Structure of the Ferryl Intermediate in the α-Ketoglutarate Dependent Non-Heme Iron Halogenase SyrB2: Contributions to H Atom Abstraction Reactivity. J. Am. Chem. Soc. 138, 5110–5122. 10.1021/jacs.6b01151. [PubMed: 27021969]
35. Que L Jr. (2007). The Road to Non-Heme Oxoferryls and Beyond. Acc. Chem. Res. 40, 493–500. 10.1021/ar700024g. [PubMed: 17595051]
36. Wang L, Gennari M, Cantú Reinhard FG, Gutiérrez J, Morozan A, Philouze C, Demeshko S, Artero V, Meyer F, de Visser SP, and Duboc C (2019). A Non-Heme Diiron Complex for (Electro)catalytic Reduction of Dioxygen: Tuning the Selectivity through Electron Delivery. J. Am. Chem. Soc. 141, 8244–8253. 10.1021/jacs.9b02011. [PubMed: 31026148]

37. Gérard EF, Yadav V, Goldberg DP, and de Visser SP (2022). What Drives Radical Halogenation versus Hydroxylation in Mononuclear Nonheme Iron Complexes? A Combined Experimental and Computational Study. J. Am. Chem. Soc. 144, 10752–10767. 10.1021/jacs.2c01375. [PubMed: 35537044]
38. Waheed SO, Ramanan R, Chaturvedi SS, Lehnert N, Schofield CJ, Christov CZ, and Karabencheva-Christova TG (2020). Role of Structural Dynamics in Selectivity and Mechanism of Non-heme Fe(II) and 2-Oxoglutarate-Dependent Oxygenases Involved in DNA Repair. ACS Cent. Sci. 6, 795–814. 10.1021/acscentsci.0c00312. [PubMed: 32490196]
39. Wong SD, Srnec M, Matthews ML, Liu LV, Kwak Y, Park K, Bell CB 3rd, Alp EE, Zhao J, Yoda Y, et al. (2013). Elucidation of the Fe (iv)=O intermediate in the catalytic cycle of the halogenase SyrB2. Nature 499, 320–323. 10.1038/nature12304. [PubMed: 23868262]
40. Fang D, Lord RL, and Cisneros GA (2013). Ab Initio QM/MM Calculations Show an Intersystem Crossing in the Hydrogen Abstraction Step in Dealkylation Catalyzed by AlkB. J. Phys. Chem. B 117, 6410–6420. 10.1021/jp403116e. [PubMed: 23642148]
41. Chaturvedi SS, Ramanan R, Hu J, Hausinger RP, and Christov CZ (2021). Atomic and Electronic Structure Determinants Distinguish between Ethylene Formation and l-Arginine Hydroxylation Reaction Mechanisms in the Ethylene-Forming Enzyme. ACS Catal. 11, 1578–1592. 10.1021/acscatal.0c03349.
42. Berger MB, Walker AR, Vázquez-Montelongo EA, and Cisneros GA (2021). Computational investigations of selected enzymes from two iron and α-ketoglutarate-dependent families. Phys. Chem. Chem. Phys. 23, 22227–22240. 10.1039/D1CP03800A. [PubMed: 34586107]
43. Chen H, Cho K-B, Lai W, Nam W, and Shaik S (2012). Dioxygen Activation by a Non-Heme Iron(II) Complex: Theoretical Study toward Understanding Ferric–Superoxo Complexes. J. Chem. Theory Comput. 8, 915–926. 10.1021/ct300015y. [PubMed: 26593354]
44. Torabifard H, and Cisneros GA (2018). Insight into wild-type and T1372E TET2-mediated 5hmC oxidation using ab initio QM/MM calculations. Chem. Sci. 9, 8433–8445. 10.1039/c8sc02961j. [PubMed: 30542593]
45. Kastner DW, Nandy A, Mehmood R, and Kulik HJ (2023). Mechanistic Insights into Substrate Positioning That Distinguish Non-heme Fe (II)/α-Ketoglutarate-Dependent Halogenases and Hydroxylases. ACS Catal. 13, 2489–2501. 10.1021/acscatal.2c06241.
46. Bassan A, Blomberg MRA, Borowski T, and Siegbahn PEM (2004). Oxygen Activation by Rieske Non-Heme Iron Oxygenases, a Theoretical Insight. J. Phys. Chem. B 108, 13031–13041. 10.1021/jp048515q.
47. Quesne MG, Latifi R, Gonzalez-Ovalle LE, Kumar D, and de Visser SP (2014). Quantum Mechanics/Molecular Mechanics Study on the Oxygen Binding and Substrate Hydroxylation Step in AlkB Repair Enzymes. Chem. Eur J. 20, 435–446. 10.1002/chem.201303282. [PubMed: 24339041]
48. Varghese A, Waheed SO, Chaturvedi SS, DiCastri I, LaRouche C, Kaski B, Lehnert N, Li D, Christov CZ, and Karabencheva-Christova TG (2023). Revealing the catalytic strategy of FTO. Chem Catal. 3, 100732. 10.1016/j.checat.2023.100732. [PubMed: 40636456]
49. Waheed SO, Chaturvedi SS, Karabencheva-Christova TG, and Christov CZ (2021). Catalytic Mechanism of Human Ten-Eleven Translocation-2 (TET2) Enzyme: Effects of Conformational Changes, Electric Field, and Mutations. ACS Catal. 11, 3877–3890. 10.1021/acscatal.0c05034.
50. Purslow JA, Nguyen TT, Khatiwada B, Singh A, and Venditti V (2021). N6-methyladenosine binding induces a metal-centered rearrangement that activates the human RNA demethylase Alkbh5. Sci. Adv. 7, eabi8215. 10.1126/sciadv.abi8215. [PubMed: 34407931]
51. Burns D, Khatiwada B, Singh A, Purslow JA, Potoyan DA, and Venditti V (2024). An α-ketoglutarate conformational switch controls iron accessibility, activation, and substrate selection of the human FTO protein. Proc. Natl. Acad. Sci. USA 121, e2404457121. 10.1073/pnas.2404457121. [PubMed: 38865275]
52. Wójcik A, Radoń M, and Borowski T (2016). Mechanism of O2 Activation by α-Ketoglutarate Dependent Oxygenases Revisited. A Quantum Chemical Study. J. Phys. Chem. A 120, 1261–1274. 10.1021/acs.jpca.5b12311. [PubMed: 26859709]

53. Bassan A, Borowski T, and Siegbahn PEM (2004). Quantum chemical studies of dioxygen activation by mononuclear non-heme iron enzymes with the 2-His-1-carboxylate facial triad. Dalton Trans. 20, 3153–3162. 10.1039/B408340G.
54. Xue J, Lu J, and Lai W (2019). Mechanistic insights into a non-heme 2-oxoglutarate-dependent ethylene-forming enzyme: selectivity of ethylene-formation versus l -Arg hydroxylation. Phys. Chem. Chem. Phys. 21, 9957–9968. 10.1039/C9CP00794F. [PubMed: 31041955]
55. Yeh C-CG, Ghafoor S, Satpathy JK, Mokkawes T, Sastri CV, and de Visser SP (2022). Cluster Model Study into the Catalytic Mechanism of α-Ketoglutarate Biodegradation by the Ethylene-Forming Enzyme Reveals Structural Differences with Nonheme Iron Hydroxylases. ACS Catal. 12, 3923–3937. 10.1021/acscatal.1c04029.
56. Kulik HJ, Blasiak LC, Marzari N, and Drennan CL (2009). First-Principles Study of Non-heme Fe(II) Halogenase SyrB2 Reactivity. J. Am. Chem. Soc. 131, 14426–14433. 10.1021/ja905206k. [PubMed: 19807187]
57. Zhang J, Li Y, Yuan W, Zhang X, Si Y, and Wang B (2024). Conformational Isomerization of the Fe(III)–OH Species Enables Selective Halogenation in Carrier-Protein-Independent Halogenase BesD and Hydroxylase-Evolved Halogenase. ACS Catal. 14, 9342–9353. 10.1021/acscatal.4c02704.
58. Grzyska PK, Appelman EH, Hausinger RP, and Proshlyakov DA (2010). Insight into the mechanism of an iron dioxygenase by resolution of steps following the FeIV═O species. Proc. Natl. Acad. Sci. USA 107, 3982–3987. 10.1073/pnas.0911565107. [PubMed: 20147623]
59. Proshlyakov DA, McCracken J, and Hausinger RP (2017). Spectroscopic Analyses of 2-Oxoglutarate-Dependent Oxygenases: TauD as a Case Study. J. Biol. Inorg. Chem. 22, 367–379. 10.1007/s00775-016-1406-3. [PubMed: 27812832]
60. Proshlyakov DA, and Hausinger RP Transient Iron Species in the Catalytic Mechanism of the Archetypal α-Ketoglutarate-Dependent Dioxygenase, TauD.
61. Galonić Fujimori D, Barr EW, Matthews ML, Koch GM, Yonce JR, Walsh CT, Bollinger JM Jr., Krebs C, and Riggs-Gelasco PJ (2007). Spectroscopic Evidence for a High-Spin Br-Fe(IV)-Oxo Intermediate in the α-Ketoglutarate-Dependent Halogenase CytC3 from Streptomyces. J. Am. Chem. Soc. 129, 13408–13409. 10.1021/ja076454e. [PubMed: 17939667]
62. Eser BE, Barr EW, Frantom PA, Saleh L, Bollinger JM Jr., Krebs C, and Fitzpatrick PF (2007). Direct Spectroscopic Evidence for a High-Spin Fe(IV) Intermediate in Tyrosine Hydroxylase. J. Am. Chem. Soc. 129, 11334–11335. 10.1021/ja074446s. [PubMed: 17715926]
63. Riggs-Gelasco PJ, Price JC, Guyer RB, Brehm JH, Barr EW, Bollinger JM Jr., and Krebs C (2004). EXAFS Spectroscopic Evidence for an Fe═O Unit in the Fe(IV) Intermediate Observed during Oxygen Activation by Taurine:α-Ketoglutarate Dioxygenase. J. Am. Chem. Soc. 126, 8108–8109. 10.1021/ja048255q. [PubMed: 15225039]
64. Krebs C, Galonić Fujimori D, Walsh CT, and Bollinger JM Jr. (2007). Non-Heme Fe(IV)–Oxo Intermediates. Acc. Chem. Res. 40, 484–492. 10.1021/ar700066p. [PubMed: 17542550]
65. Solomon EI, Light KM, Liu LV, Srnec M, and Wong SD (2013). Geometric and Electronic Structure Contributions to Function in Non-Heme Iron Enzymes. Acc. Chem. Res. 46, 2725–2739. 10.1021/ar400149m. [PubMed: 24070107]
66. Solomon EI, Brunold TC, Davis MI, Kemsley JN, Lee SK, Lehnert N, Neese F, Skulan AJ, Yang YS, and Zhou J (2000). Geometric and electronic structure/function correlations in non-heme iron enzymes. Chem. Rev. 100, 235–350. 10.1021/cr9900275. [PubMed: 11749238]
67. Toh JDW, Crossley SWM, Bruemmer KJ, Ge EJ, He D, Iovan DA, and Chang CJ (2020). Distinct RNA N-demethylation pathways catalyzed by nonheme iron ALKBH5 and FTO enzymes enable regulation of formaldehyde release rates. Proc. Natl. Acad. Sci. USA 117, 25284–25292. 10.1073/pnas.2007349117. [PubMed: 32989163]
68. Feng C, Liu Y, Wang G, Deng Z, Zhang Q, Wu W, Tong Y, Cheng C, and Chen Z (2014). Crystal Structures of the Human RNA Demethylase Alkbh5 Reveal Basis for Substrate Recognition. J. Biol. Chem. 289, 11571–11583. 10.1074/jbc.M113.546168. [PubMed: 24616105]
69. A M, M R, A DD, G C, M M, V Z, and G N (2020). 3D proteome-wide scale screening and activity evaluation of a new ALKBH5 inhibitor in U87 glioblastoma cell line. Bioorg. Med. Chem. 28, 115300. 10.1016/j.bmc.2019.115300. [PubMed: 31937477]

70. Lai G-Q, Li Y, Zhu H, Zhang T, Gao J, Zhou H, and Yang C-G (2024). A covalent compound selectively inhibits RNA demethylase ALKBH5 rather than FTO. RSC Chem. Biol. 5, 335–343. 10.1039/D3CB00230F. [PubMed: 38576724]
71. Fang Z, Mu B, Liu Y, Guo N, Xiong L, Guo Y, Xia A, Zhang R, Zhang H, Yao R, et al. (2022). Discovery of a potent, selective and cell active inhibitor of m6A demethylase ALKBH5. Eur. J. Med. Chem. 238, 114446. 10.1016/j.ejmech.2022.114446. [PubMed: 35597008]
72. Wang Y-Z, Li H-Y, Zhang Y, Jiang R-X, Xu J, Gu J, Jiang Z, Jiang Z-Y, You Q-D, and Guo X-K (2023). Discovery of Pyrazolo [1,5-a]pyrimidine Derivative as a Novel and Selective ALKBH5 Inhibitor for the Treatment of AML. J. Med. Chem. 66, 15944–15959. 10.1021/acs.jmedchem.3c01374. [PubMed: 37983486]
73. Takahashi H, Hase H, Yoshida T, Tashiro J, Hirade Y, Kitae K, and Tsujikawa K (2022). Discovery of two novel ALKBH5 selective inhibitors that exhibit uncompetitive or competitive type and suppress the growth activity of glioblastoma multiforme. Chem. Biol. Drug Des. 100, 1–12. 10.1111/cbdd.14051. [PubMed: 35384315]
74. Selberg S, Seli N, Kankuri E, and Karelson M (2021). Rational Design of Novel Anticancer Small-Molecule RNA m6A Demethylase ALKBH5 Inhibitors. ACS Omega 6, 13310–13320. 10.1021/acsomega.1c01289. [PubMed: 34056479]
75. Ye S, Riplinger C, Hansen A, Krebs C, Bollinger JM Jr., and Neese F (2012). Electronic Structure Analysis of the Oxygen-Activation Mechanism by FeII- and α-Ketoglutarate (αKG)-Dependent Dioxygenases. Chem. Eur J. 18, 6555–6567. 10.1002/chem.201102829. [PubMed: 22511515]
76. Thomas MG, Jaber Sathik Rifayee SB, and Christov CZ (2024). How Do Variants of Residues in the First Coordination Sphere, Second Coordination Sphere, and Remote Areas Influence the Catalytic Mechanism of Non-Heme Fe(II)/2-Oxoglutarate Dependent Ethylene-Forming Enzyme? ACS Catal. 14, 18550–18569. 10.1021/acscatal.4c04010. [PubMed: 39722885]
77. Ramanan R, Chaturvedi SS, Lehnert N, Schofield CJ, Karabencheva-Christova TG, and Christov CZ (2020). Catalysis by the JmjC histone demethylase KDM4A integrates substrate dynamics, correlated motions and molecular orbital control. Chem. Sci. 11, 9950–9961. 10.1039/D0SC03713C. [PubMed: 34094257]
78. Smith AJT, Müller R, Toscano MD, Kast P, Hellinga HW, Hilvert D, and Houk KN (2008). Structural reorganization and preorganization in enzyme active sites: comparisons of experimental and theoretically ideal active site geometries in the multistep serine esterase reaction cycle. J. Am. Chem. Soc. 130, 15361–15373. 10.1021/ja803213p. [PubMed: 18939839]
79. Wang B, Cao Z, Sharon DA, and Shaik S (2015). Computations Reveal a Rich Mechanistic Variation of Demethylation of N-methylated DNA/RNA Nucleotides by FTO. ACS Catal. 5, 7077–7090. 10.1021/acscatal.5b01867.
80. Nashine VC, Hammes-Schiffer S, and Benkovic SJ (2010). Coupled motions in enzyme catalysis. Curr. Opin. Chem. Biol. 14, 644–651. 10.1016/j.cbpa.2010.07.020. [PubMed: 20729130]
81. Rabe P, Kamps JJAG, Sutherlin KD, Linyard JDS, Aller P, Pham CC, Makita H, Clifton I, McDonough MA, Leissing TM, et al. (2021). X-ray free-electron laser studies reveal correlated motion during isopenicillin N synthase catalysis. Sci. Adv. 7, eabh0250. 10.1126/sciadv.abh0250. [PubMed: 34417180]
82. Luo J, and Bruice TC (2004). Anticorrelated motions as a driving force in enzyme catalysis: The dehydrogenase reaction. Proc. Natl. Acad. Sci. USA 101, 13152–13156. 10.1073/pnas.0405502101. [PubMed: 15331786]
83. Xu D, Meisburger SP, and Ando N (2021). Correlated Motions in Structural Biology. Biochemistry 60, 2331–2340. 10.1021/acs.biochem.1c00420. [PubMed: 34291898]
84. Shaik S, Chen H, and Janardanan D (2011). Exchange-enhanced reactivity in bond activation by metal–oxo enzymes and synthetic reagents. Nat. Chem. 3, 19–27. 10.1038/nchem.943. [PubMed: 21160512]
85. Shaik S, Hirao H, and Kumar D (2007). Reactivity of High-Valent Iron–Oxo Species in Enzymes and Synthetic Reagents: A Tale of Many States. Acc. Chem. Res. 40, 532–542. 10.1021/ar600042c. [PubMed: 17488054]

86. Hirao H, Kumar D, Que L Jr., and Shaik S (2006). Two-State Reactivity in Alkane Hydroxylation by Non-Heme Iron−Oxo Complexes. J. Am. Chem. Soc. 128, 8590–8606. 10.1021/ja061609o. [PubMed: 16802826]
87. Hirao H, Kumar D, Thiel W, and Shaik S (2005). Two States and Two More in the Mechanisms of Hydroxylation and Epoxidation by Cytochrome P450. J. Am. Chem. Soc. 127, 13007–13018. 10.1021/ja053847+. [PubMed: 16159296]
88. Solomon EI (2001). Geometric and Electronic Structure Contributions to Function in Bioinorganic Chemistry: Active Sites in Non-Heme Iron Enzymes. Inorg. Chem. 40, 3656–3669. 10.1021/ic010348a. [PubMed: 11442362]
89. Waheed SO, Ramanan R, Chaturvedi SS, Ainsley J, Evison M, Ames JM, Schofield CJ, Christov CZ, and Karabencheva-Christova TG (2019). Conformational flexibility influences structure–function relationships in nucleic acid N -methyl demethylases. Org. Biomol. Chem. 17, 2223–2231. 10.1039/C9OB00162J. [PubMed: 30720838]
90. Waheed SO, Varghese A, DiCastri I, Kaski B, LaRouche C, Fields GB, and Karabencheva-Christova TG (2023). Mechanism of the Early Catalytic Events in the Collagenolysis by Matrix Metalloproteinase-1. ChemPhysChem 24, e202200649. 10.1002/cphc.202200649. [PubMed: 36161746]
91. Barducci A, Bonomi M, and Parrinello M (2011). Metadynamics. WIREs Comput. Mol. Sci. 1, 826–843. 10.1002/wcms.31.
92. Gorantla KR, Krishnan A, Waheed SO, Varghese A, DiCastri I, LaRouche C, Paik M, Fields GB, and Karabencheva-Christova TG (2024). Novel Insights into the Catalytic Mechanism of Collagenolysis by Zn(II)-Dependent Matrix Metalloproteinase-1. Biochemistry 63, 1925–1940. 10.1021/acs.biochem.4c00076. [PubMed: 38963231]
93. Soriano A, Castillo R, Christov C, Andrés J, Moliner V, and Tuñón I (2006). Catalysis in glycine N-methyltransferase: testing the electrostatic stabilization and compression hypothesis. Biochemistry 45, 14917–14925. 10.1021/bi061319k. [PubMed: 17154529]
94. Martí S, Roca M, Andrés J, Moliner V, Silla E, Tuñón I, and Bertrán J (2004). Theoretical insights in enzyme catalysis. Chem. Soc. Rev. 33, 98–107. 10.1039/B301875J. [PubMed: 14767505]
95. Mauer J, Luo X, Blanjoie A, Jiao X, Grozhik AV, Patil DP, Linder B, Pickering BF, Vasseur J-J, Chen Q, et al. (2017). Reversible methylation of m6Am in the 5′ cap controls mRNA stability. Nature 541, 371–375. 10.1038/nature21022. [PubMed: 28002401]
96. Hu L, Lu J, Cheng J, Rao Q, Li Z, Hou H, Lou Z, Zhang L, Li W, Gong W, et al. (2015). Structural insight into substrate preference for TET-mediated oxidation. Nature 527, 118–122. 10.1038/nature15713. [PubMed: 26524525]
97. Zhang M, Yang S, Nelakanti R, Zhao W, Liu G, Li Z, Liu X, Wu T, Xiao A, and Li H (2020). Mammalian ALKBH1 serves as an N6-mA demethylase of unpairing DNA. Cell Res. 30, 197–210. 10.1038/s41422-019-0237-5. [PubMed: 32051560]
98. Roy TW, and Bhagwat AS (2007). Kinetic studies of Escherichia coli AlkB using a new fluorescence-based assay for DNA demethylation. Nucleic Acids Res. 35, e147. 10.1093/nar/gkm1031. [PubMed: 18003660]
99. Price JC, Barr EW, Tirupati B, Bollinger JM, and Krebs C (2003). The first direct characterization of a high-valent iron intermediate in the reaction of an alpha-ketoglutarate-dependent dioxygenase: a high-spin FeIV complex in taurine/alpha-ketoglutarate dioxygenase (TauD) from Escherichia coli. Biochemistry 42, 7497–7508. 10.1021/bi030011f. [PubMed: 12809506]
100. Godfrey E, Porro CS, and de Visser SP (2008). Comparative Quantum Mechanics/Molecular Mechanics (QM/MM) and Density Functional Theory Calculations on the Oxo−Iron Species of Taurine/α-Ketoglutarate Dioxygenase. J. Phys. Chem. A 112, 2464–2468. 10.1021/jp710999v. [PubMed: 18237159]
101. Álvarez-Barcia S, and Kästner J (2017). Atom Tunneling in the Hydroxylation Process of Taurine/α-Ketoglutarate Dioxygenase Identified by Quantum Mechanics/Molecular Mechanics Simulations. J. Phys. Chem. B 121, 5347–5354. 10.1021/acs.jpcb.7b03477. [PubMed: 28490178]
102. Liu H, Llano J, and Gauld JW (2009). A DFT Study of Nucleobase Dealkylation by the DNA Repair Enzyme AlkB. J. Phys. Chem. B 113, 4887–4898. 10.1021/jp810715t. [PubMed: 19338370]

103. Rifayee SBJS, Chaturvedi SS, Warner C, Wildey J, White W, Thompson M, Schofield CJ, and Christov CZ (2023). Catalysis by KDM6 Histone Demethylases – A Synergy between the Non-Heme Iron(II) Center, Second Coordination Sphere, and Long-Range Interactions. Chem. Eur J. 29, e202301305. 10.1002/chem.202301305. [PubMed: 37258457]
104. Thomas MG, Jaber Sathik Rifayee SB, Chaturvedi SS, Gorantla KR, White W, Wildey J, Schofield CJ, and Christov CZ (2024). The Unique Role of the Second Coordination Sphere to Unlock and Control Catalysis in Nonheme Fe(II)/2-Oxoglutarate Histone Demethylase KDM2A. Inorg. Chem. 63, 10737–10755. 10.1021/acs.inorgchem.4c01365. [PubMed: 38781256]
105. Siegbahn PEM (2023). How Protons Move in Enzymes—The Case of Nitrogenase. J. Phys. Chem. B 127, 2156–2159. 10.1021/acs.jpcb.2c08567. [PubMed: 36862530]
106. Stuchebrukhov AA (2009). Mechanisms of proton transfer in proteins: Localized charge transfer versus delocalized soliton transfer. Phys. Rev. E 79, 031927. 10.1103/PhysRevE.79.031927.
107. Sen K, and Hackett JC (2010). Peroxo−Iron Mediated Deformylation in Sterol 14α-Demethylase Catalysis. J. Am. Chem. Soc. 132, 10293–10305. 10.1021/ja906192b. [PubMed: 20662512]
108. Mokkawes T, Lim ZQ, and de Visser SP (2022). Mechanism of Melatonin Metabolism by CYP1A1: What Determines the Bifurcation Pathways of Hydroxylation versus Deformylation? J. Phys. Chem. B 126, 9591–9606. 10.1021/acs.jpcb.2c07200. [PubMed: 36380557]
109. Fu Y, Jia G, Pang X, Wang RN, Wang X, Li CJ, Smemo S, Dai Q, Bailey KA, Nobrega MA, et al. (2013). FTO-mediated formation of N6-hydroxymethyladenosine and N6-formyladenosine in mammalian RNA. Nat. Commun. 4, 1798. 10.1038/ncomms2822. [PubMed: 23653210]
110. Frisch MJ, Trucks GW, Schlegel HB, Scuseria GE, Robb MA, Cheeseman JR, Scalmani G, Barone V, Petersson GA, Nakatsuji H, et al. (2016). Gaussian 16 (Rev. C.01).
111. Olsson MHM, Søndergaard CR, Rostkowski M, and Jensen JH (2011). PROPKA3: Consistent Treatment of Internal and Surface Residues in Empirical pKa Predictions. J. Chem. Theory Comput. 7, 525–537. 10.1021/ct100578z. [PubMed: 26596171]
112. Pettersen EF, Goddard TD, Huang CC, Couch GS, Greenblatt DM, Meng EC, and Ferrin TE (2004). UCSF Chimera–a visualization system for exploratory research and analysis. J. Comput. Chem. 25, 1605–1612. 10.1002/jcc.20084. [PubMed: 15264254]
113. Wang J, Wang W, Kollman PA, and Case DA (2006). Automatic atom type and bond type perception in molecular mechanical calculations. J. Mol. Graph. Model. 25, 247–260. 10.1016/j.jmgm.2005.12.005. [PubMed: 16458552]
114. Li P, and Merz KM Jr. (2016). MCPB.py: A Python Based Metal Center Parameter Builder. J. Chem. Inf. Model. 56, 599–604. 10.1021/acs.jcim.5b00674. [PubMed: 26913476]
115. Seminario JM (1996). Calculation of intramolecular force fields from second-derivative tensors. Int. J. Quantum Chem. 60, 1271–1277. 10.1002/(SICI)1097-461X(1996)60:7<1271::AID-QUA8>3.0.CO;2-W.
116. Woods RJ, and Chappelle R (2000). Restrained electrostatic potential atomic partial charges for condensed-phase simulations of carbohydrates. THEOCHEM 527, 149–156. 10.1016/S0166-1280(00)00487-5. [PubMed: 25309012]
117. Maier JA, Martinez C, Kasavajhala K, Wickstrom L, Hauser KE, and Simmerling C (2015). ff14SB: Improving the Accuracy of Protein Side Chain and Backbone Parameters from ff99SB. J. Chem. Theory Comput. 11, 3696–3713. 10.1021/acs.jctc.5b00255. [PubMed: 26574453]
118. Jorgensen WL, Chandrasekhar J, Madura JD, Impey RW, and Klein ML (1983). Comparison of simple potential functions for simulating liquid water. J. Chem. Phys. 79, 926–935. 10.1063/1.445869.
119. Davidchack RL, Handel R, and Tretyakov MV (2009). Langevin thermostat for rigid body dynamics. J. Chem. Phys. 130, 234101. 10.1063/1.3149788. [PubMed: 19548705]
120. Bresme F (2001). Equilibrium and nonequilibrium molecular-dynamics simulations of the central force model of water. J. Chem. Phys. 115, 7564–7574. 10.1063/1.1407288.
121. Ryckaert J-P, Ciccotti G, and Berendsen HJC (1977). Numerical Integration of the Cartesian Equations of Motion of a System with Constraints: Molecular Dynamics of n-Alkanes. J. Comput. Phys. 23, 327–341. 10.1016/0021-9991(77)90098-5.
122. Darden T, York D, and Pedersen L (1993). Particle mesh Ewald: An N·log(N) method for Ewald sums in large systems. J. Chem. Phys. 98, 10089–10092. 10.1063/1.464397.

123. Roe DR, and Cheatham TE 3rd. (2013). PTRAJ and CPPTRAJ: Software for Processing and Analysis of Molecular Dynamics Trajectory Data. J. Chem. Theory Comput. 9, 3084–3095. 10.1021/ct400341p. [PubMed: 26583988]

124. Grant BJ, Rodrigues APC, ElSawy KM, McCammon JA, and Caves LSD (2006). Bio3d: an R package for the comparative analysis of protein structures. Bioinforma. Oxf. Engl. 22, 2695–2696. 10.1093/bioinformatics/btl461.

125. Metz S, Kästner J, Sokol AA, Keal TW, and Sherwood P (2014). ChemShell—a modular software package for QM/MM simulations. WIREs Comput. Mol. Sci. 4, 101–110. 10.1002/wcms.1163.

126. Ahlrichs R, Bär M, Häser M, Horn H, and Kölmel C (1989). Electronic structure calculations on workstation computers: The program system turbomole. Chem. Phys. Lett. 162, 165–169. 10.1016/0009-2614(89)85118-8.

127. Smith W, and Forester TR (1996). DL_POLY_2.0: A general-purpose parallel molecular dynamics simulation package. J. Mol. Graph. 14, 136–141. 10.1016/S0263-7855(96)00043-4. [PubMed: 8901641]

128. Singh UC, and Kollman PA (1986). A combined ab initio quantum mechanical and molecular mechanical method for carrying out simulations on complex molecular systems: Applications to the CH3Cl + Cl− exchange reaction and gas phase protonation of polyethers. J. Comput. Chem. 7, 718–730. 10.1002/jcc.540070604.

129. Kästner J, Carr JM, Keal TW, Thiel W, Wander A, and Sherwood P (2009). DL-FIND: An Open-Source Geometry Optimizer for Atomistic Simulations. J. Phys. Chem. A 113, 11856–11865. 10.1021/jp9028968. [PubMed: 19639948]

130. Henkelman G, and Jónsson H (1999). A dimer method for finding saddle points on high dimensional potential surfaces using only first derivatives. J. Chem. Phys. 111, 7010–7022. 10.1063/1.480097.

131. Sheong F, Zhang J-X, and Lin Z (2019). Revitalizing Spin Natural Orbital Analysis: Electronic Structures of Mixed-Valence Compounds, Singlet Biradicals, and Antiferromagnetically Coupled Systems. J. Comput. Chem. 40, 1172–1184. 10.1002/jcc.25762. [PubMed: 30652332]

132. Graham SE, Syeda F, and Cisneros GA (2012). Computational Prediction of Residues Involved in Fidelity Checking for DNA Synthesis in DNA Polymerase I. Biochemistry 51, 2569–2578. 10.1021/bi201856m. [PubMed: 22397306]

Highlights

- The complete mechanism of ALKBH5 with m^6A-ssRNA substrate has been explored
- Post-hydroxylation in ALKBH5 follows a proton transfer pathway
- Key role of SCS residues Lys132 and Tyr139 in post-hydroxylation has been revealed
- Study proposes key correlated motions linked to ALKBH5's demethylation activity

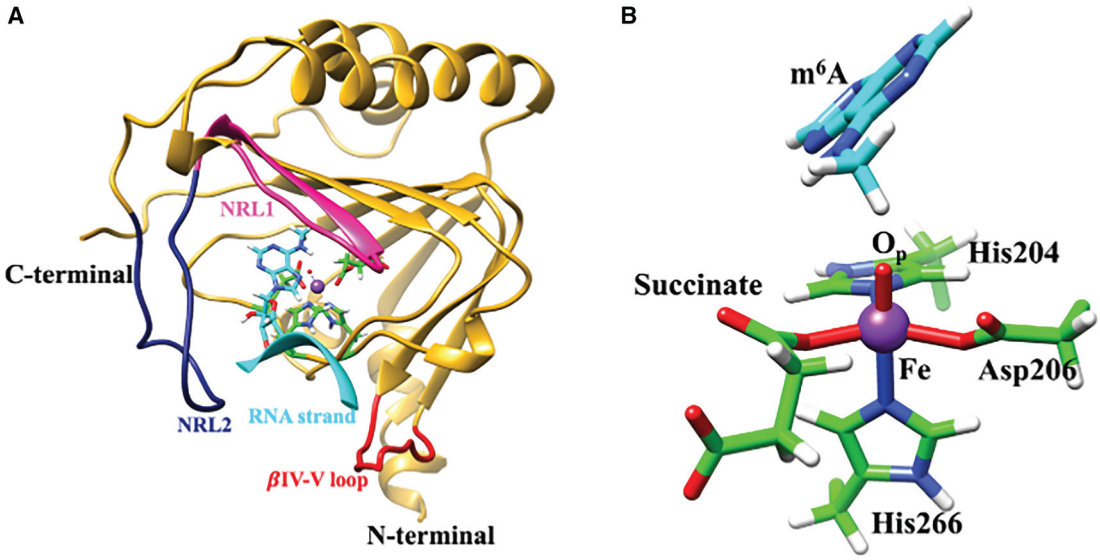

Figure 1. Structural considerations

(A) ALKBH5-ssRNA complex crystal structure (PDB ID: 7WKV). The ssRNA is shown in cyan; nucleotide recognition lids, NRL1 and NRL2, are colored in pink and navy blue, respectively, and the βIV-V loop is highlighted in red.

(B) Active site zoomed-in view of the Fe(IV)=O center; the model is based on the same crystal structure (PDB ID: 7WKV)[17,18] with the metal center replaced from Mn to Fe.

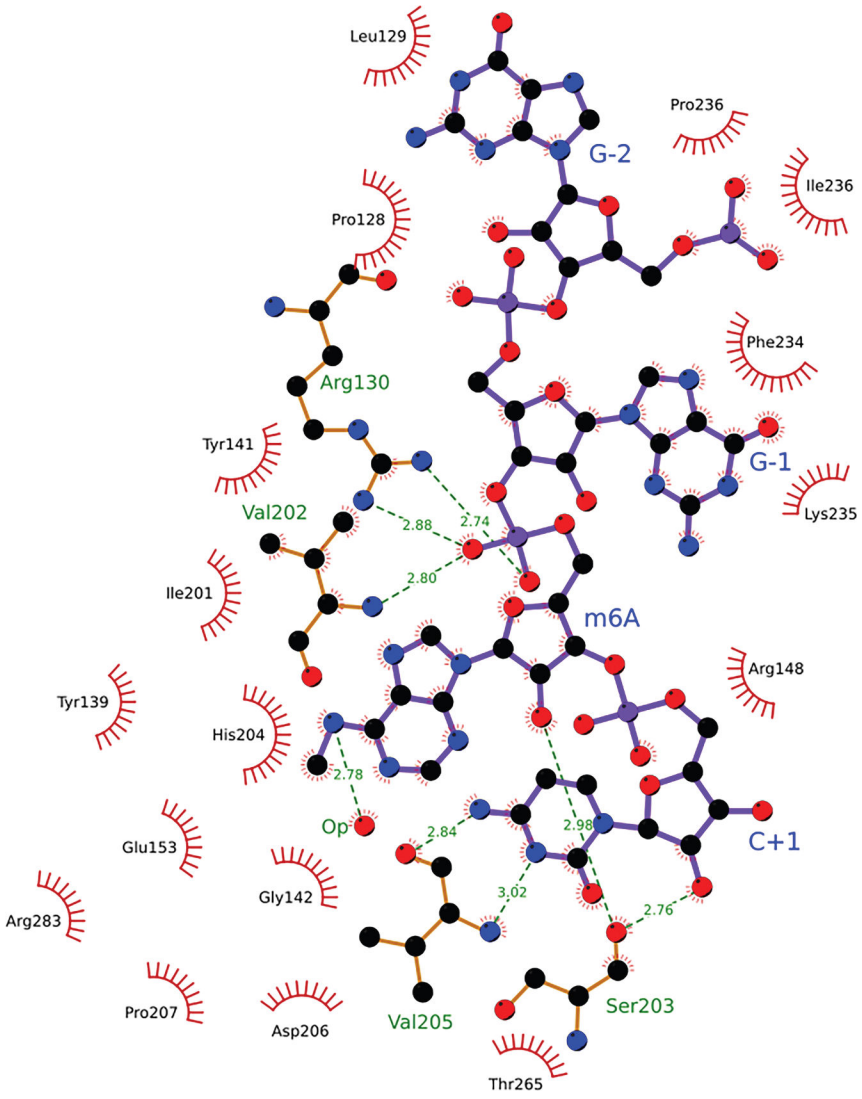

Figure 2. Two-dimensional interaction network of the ssRNA substrate and the ALKBH5 residues

Hydrogen bond distances are in Å. PDB ID: 7WKV[17,18]

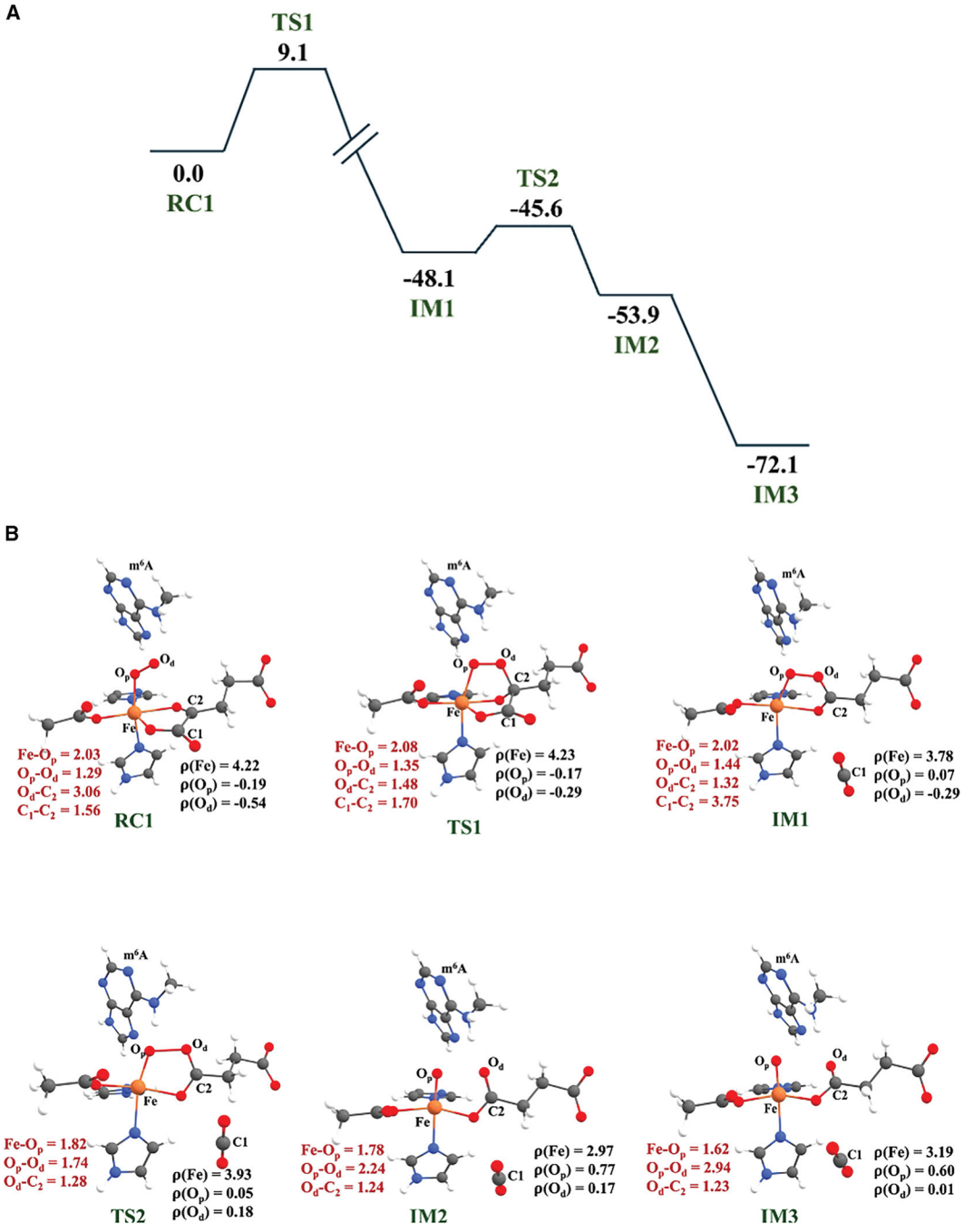

Figure 3. Dioxygen activation mechanism

(A) QM/MM minimum energy profile for O_2 activation reaction of the ALKBH5-Fe(III)–O–$O^{\cdot -}$ m^6A (ssRNA) complex (RC1). Relative energies are given in kcal/mol at the B3 level (in black).

(B) Geometries of the stationary points during the O_2 activation reaction. Significant distances (Å) and spin densities are in red and black, respectively.

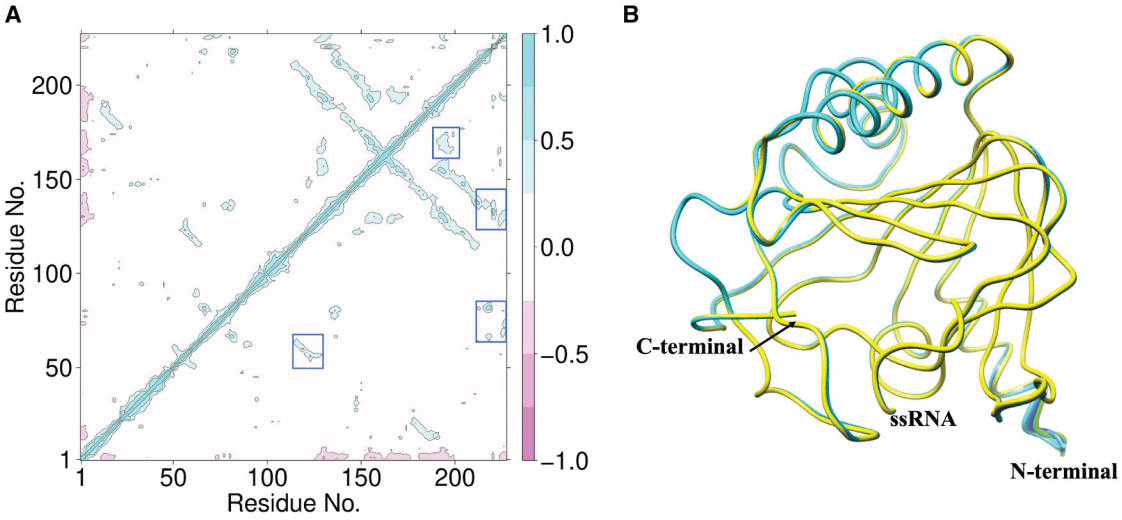

Figure 4. Conformational dynamics

(A) Dynamic cross-correlation analysis (DCCA) of the ALKBH5-ssRNA ferryl complex. The numbers from 1 to 226 correspond to 74–299 in the crystal structure—PDB ID: 7WKV. 1–219 (protein), 220 (Fe), 221(O_p), 222 (succinate), 223–226 (ssRNA), and 225 (m^6A).

(B) Principal-component analysis (PCA) of Cα atoms in the ALKBH5-ssRNA ferryl complex. The principal direction of motion of the residues is shown by color change from yellow to blue.

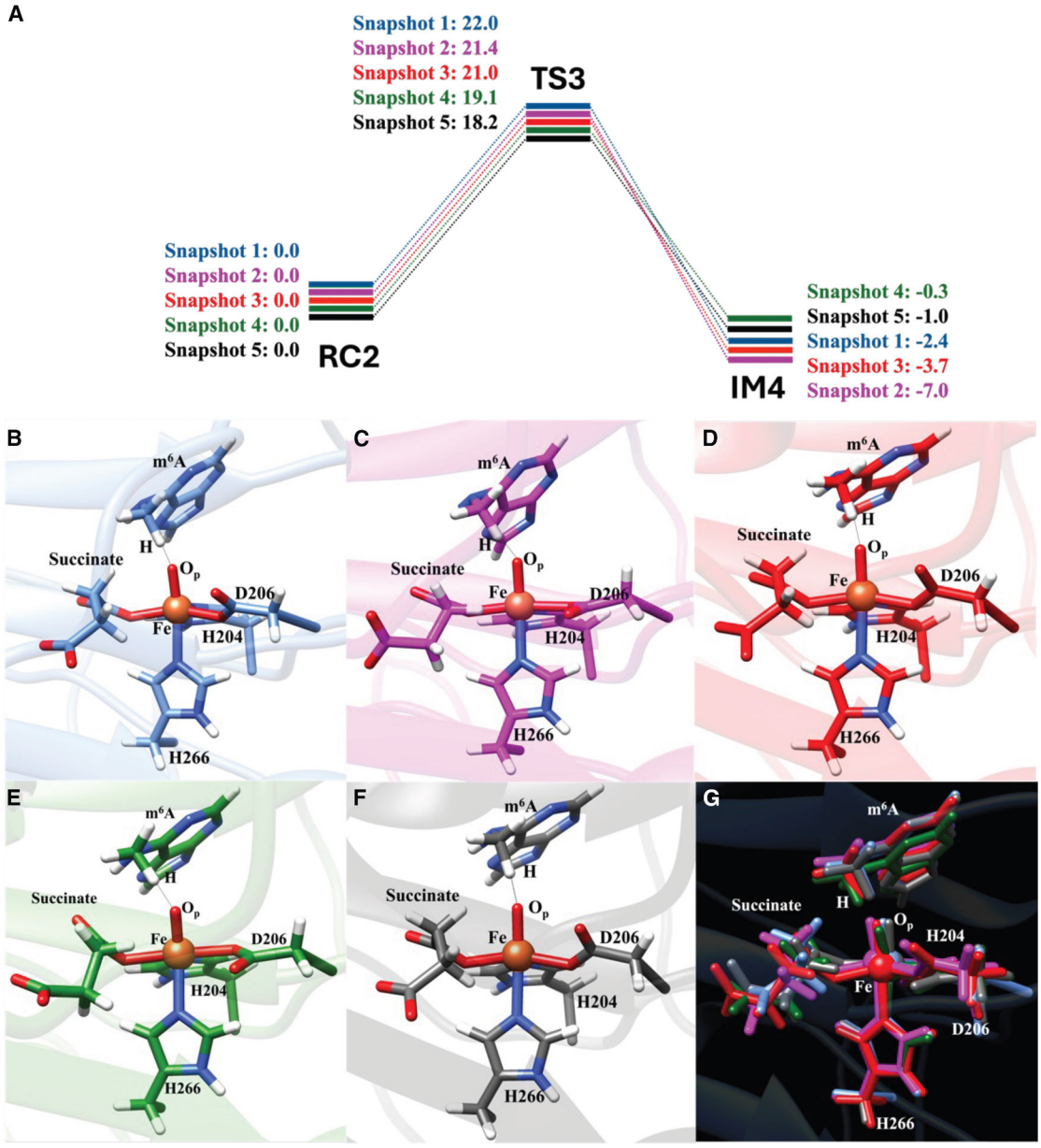

Figure 5. Hydrogen atom transfer

(A) The reaction profile of the HAT in ALKBH5 calculated using five different RC2 structures obtained as snapshots from the MD simulation. Relative energies are provided in kcal/mol at the B3 level.

(B–F) QM/MM optimized geometries of the TSs from the five HAT reaction profiles: (B) reaction profile 1, (C) reaction profile 2, (D) reaction profile 3, (E) reaction profile 4, and (F) reaction profile 5.

(G) Superimposed image of all five TSs.

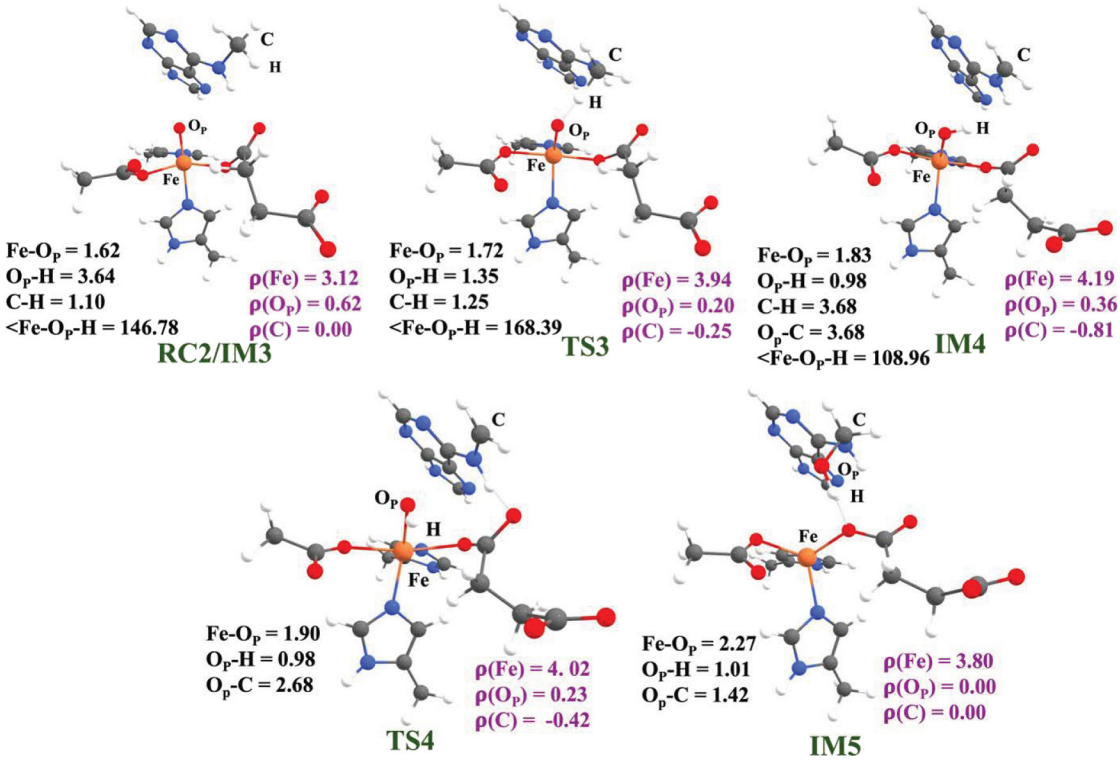

Figure 6. Optimized geometries of stationary points in the HAT and rebound hydroxylation steps in ALKBH5-ssRNA

Key geometric parameters (distance in Å, and angle in degrees) and spin densities (ρ) are in black and pink, respectively.

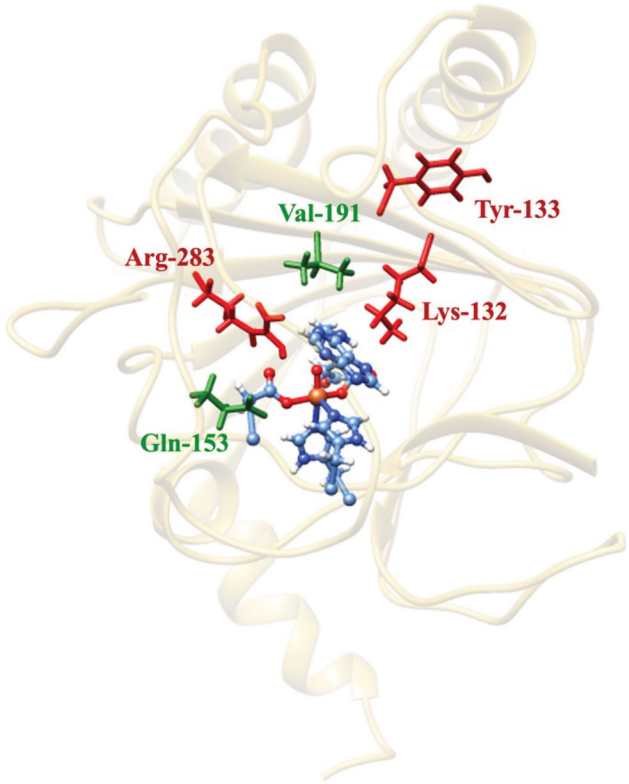

Figure 7. Key residues in HAT

Primary residues stabilizing (green) and destabilizing (red) HAT TS (TS3).

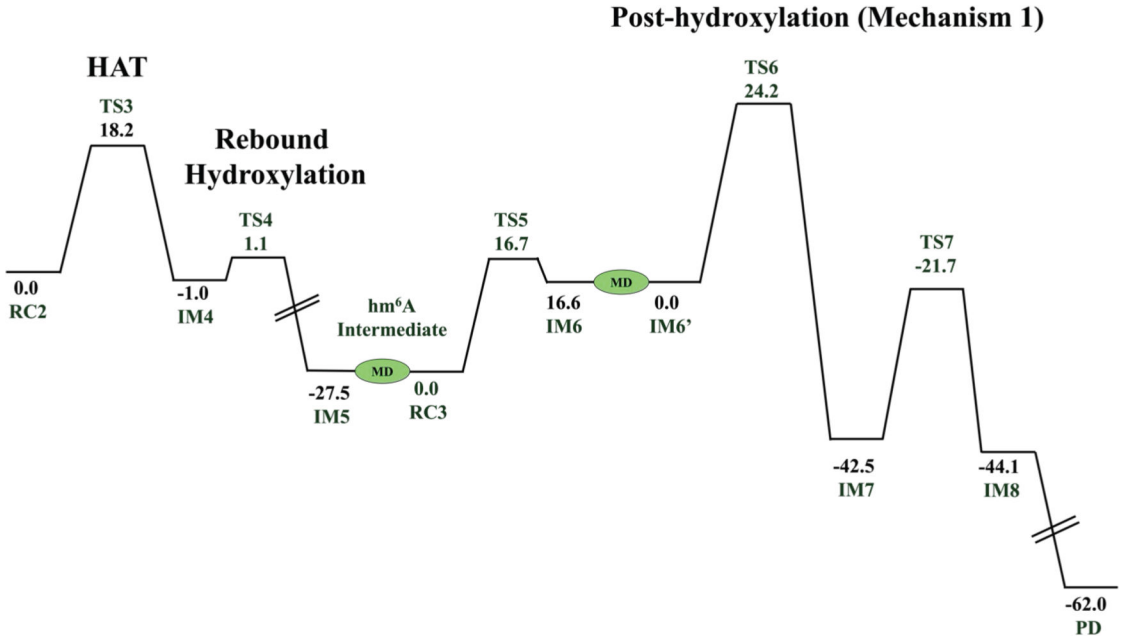

Figure 8. QM/MM energy profile of HAT, rebound hydroxylation, and the post-hydroxylation (mechanism 1) reactions by ALKBH5-ssRNA

Relative energies are in kcal/mol at B2, with ZPE (B3) in black.

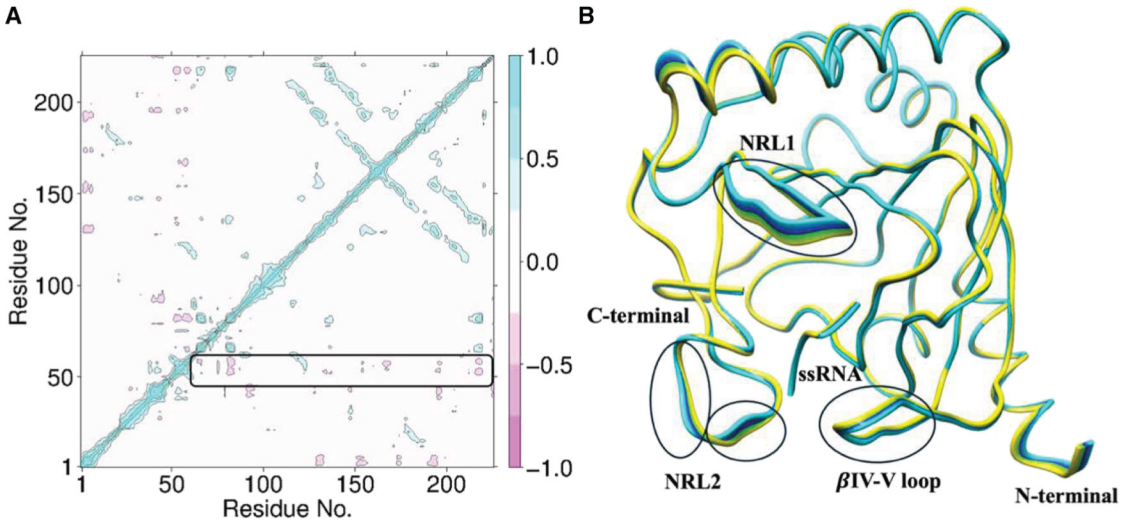

Figure 9. Conformational dynamics of the hm^{6}A intermediate

(A) Dynamic cross-correlation analysis (DCCA) of the ALKBH5-ssRNA hm^{6}A complex. The numbers from 1 to 226 correspond to 74–299 in the crystal structure (PDB ID: 7WKV): 1–219 (protein), 220 (Fe), 221 (succinate), 222–225 (RNA), and 224 (hm^{6}A).

(B) Principal-component analysis (PCA) of Cα atoms in the ALKBH5-ssRNA hm^{6}A complex. The principal direction of motion of the residues is shown by color change from yellow to blue.

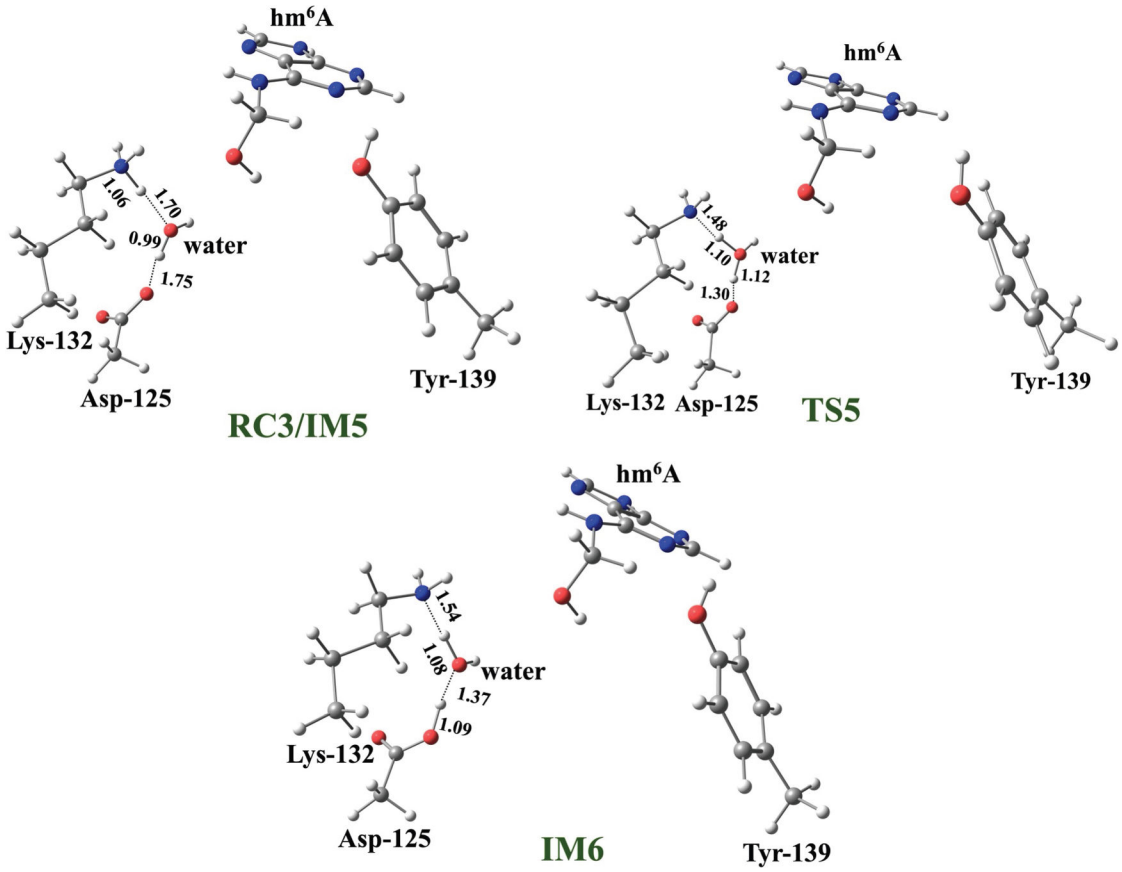

Figure 10. Optimized geometries of the stationary points involved in post-hydroxylation steps (mechanism 1)

Distances (in Å) are given in black.

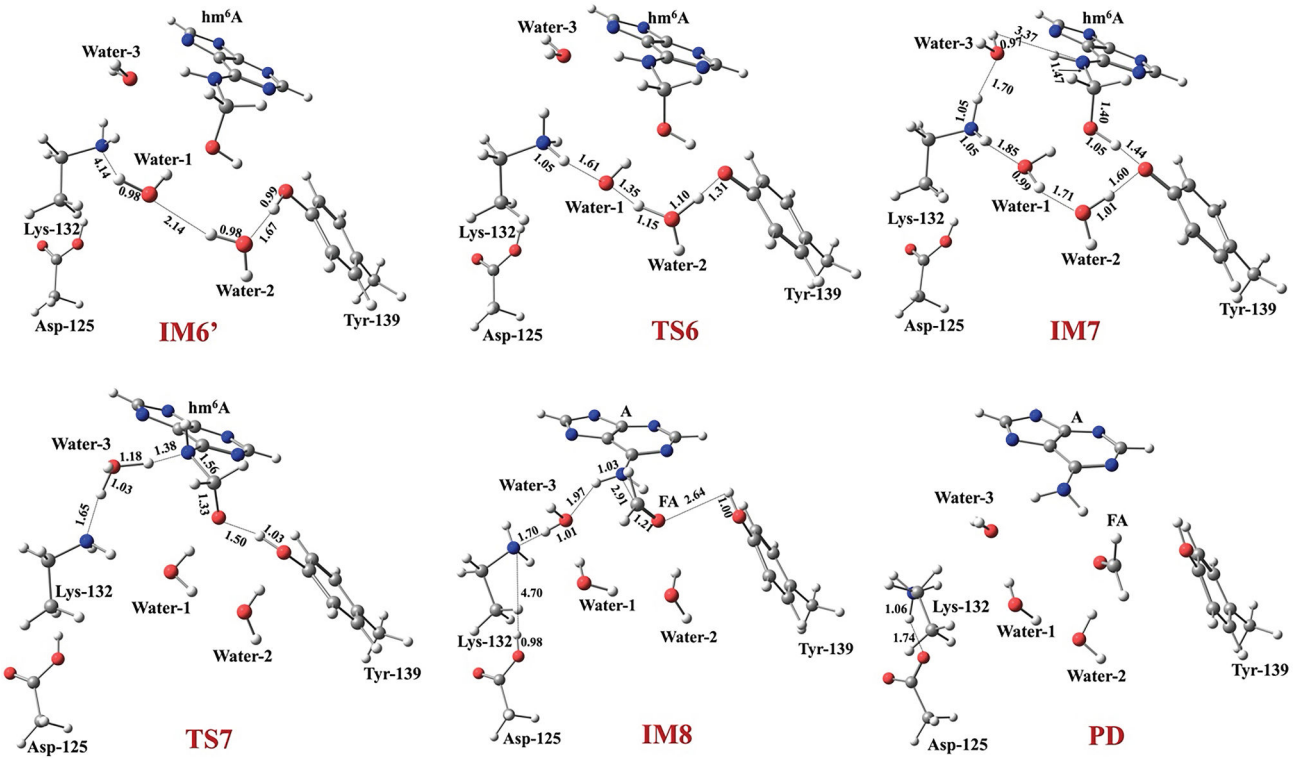

Figure 11. Optimized geometries of the stationary points in the post-hydroxylation reaction by mechanism 1

Significant distances (in Å) are given in black.

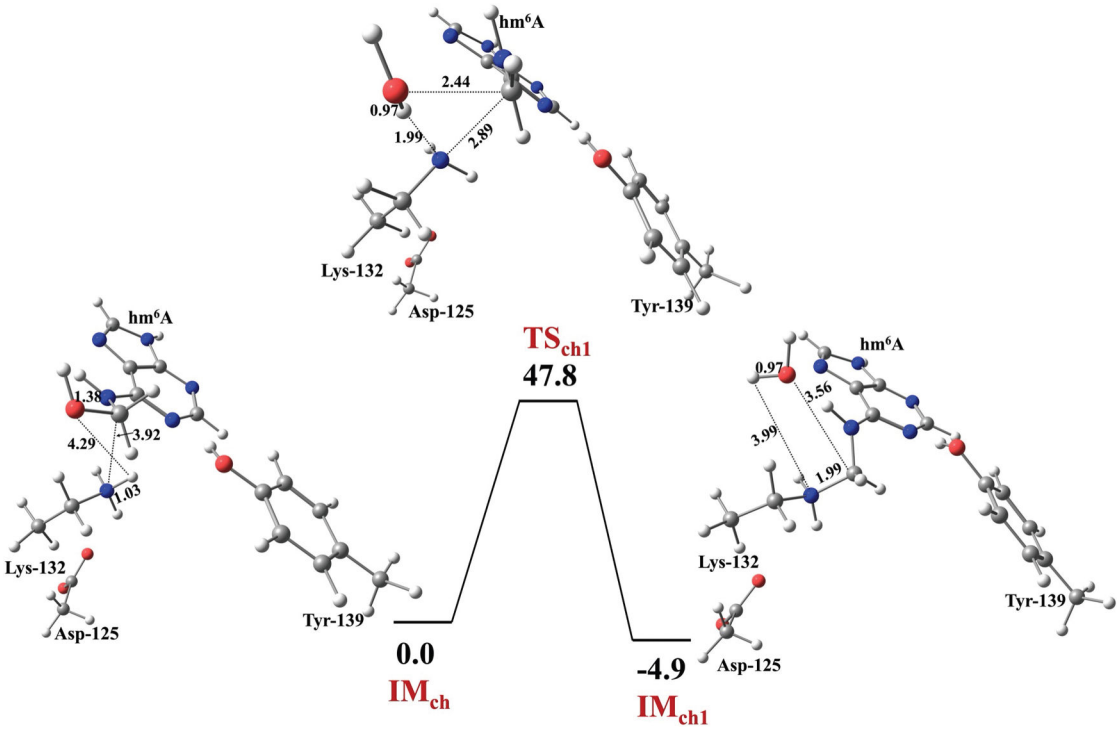

Figure 12. QM/MM energy profile of Lys132-protein-substrate intermediate formation via suprafacial displacement (as in Scheme S2) reaction by ALKBH5-ssRNA

Relative energies are in kcal/mol at the B3 level. For further information, an additional ChemDraw image of the IM_{ch} is provided in Figure S22.

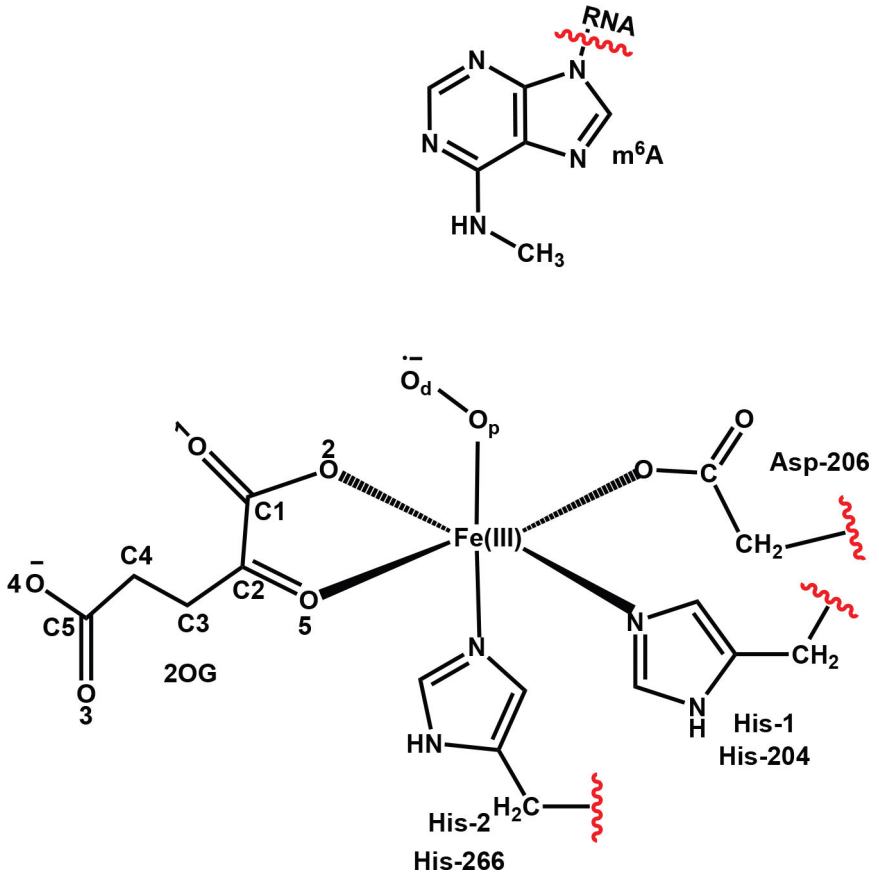

Figure 13. The active site of ALKBH5 is included in the QM region for QM/MM calculations of O_2 activation

The red squiggly lines indicate the QM/MM region boundary where the hydrogen link atom would connect.

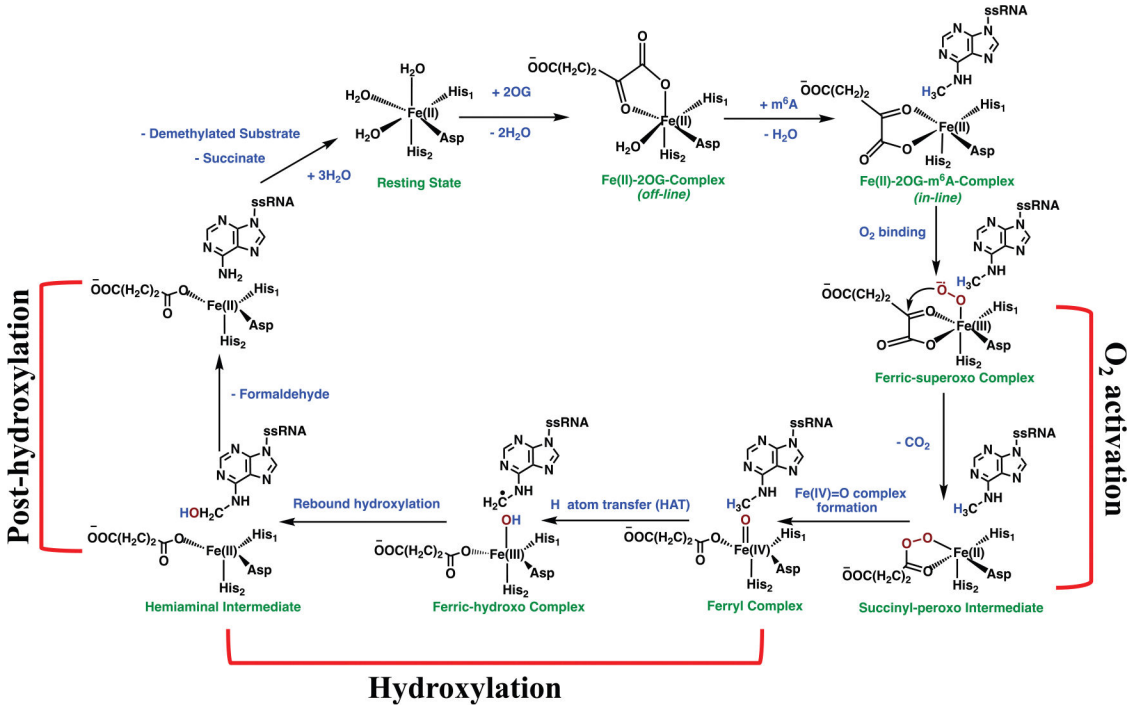

Scheme 1. Proposed catalytic mechanism for ALKBH5

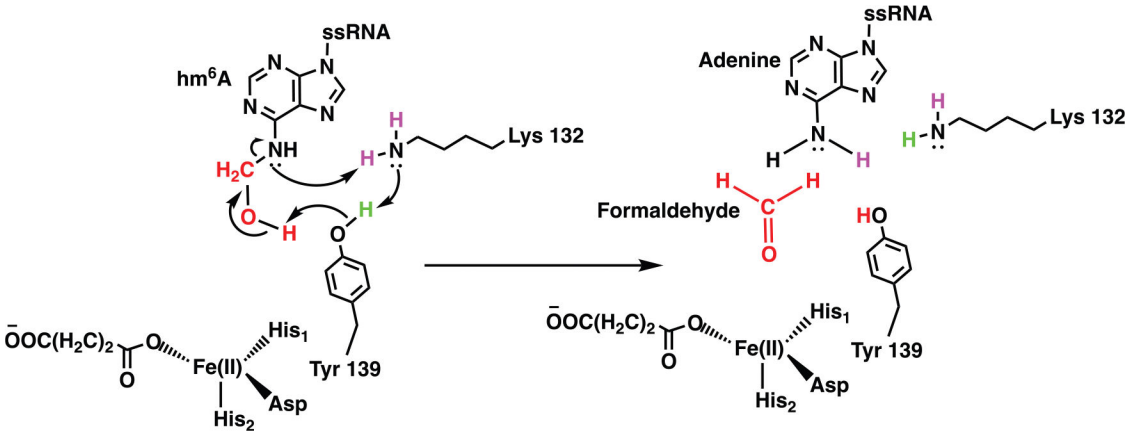

Scheme 2. Proposed mechanism of ALKBH5-mediated post-hydroxylation of hm^{6}A through a series of proton transfers

Mechanism 1.[18]

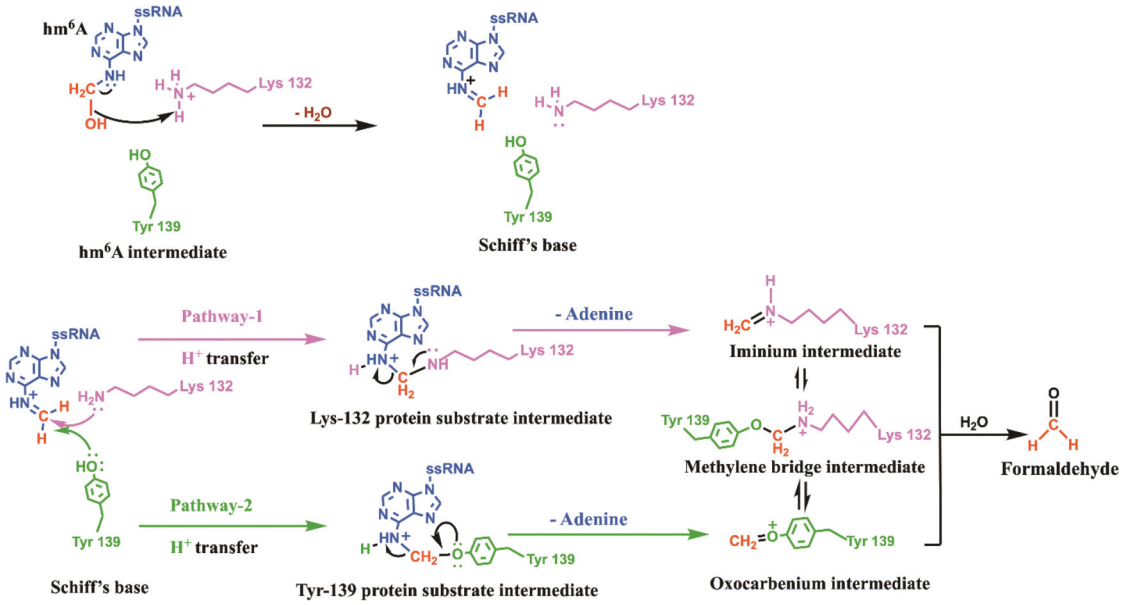

Scheme 3. Proposed mechanism of ALKBH5-mediated post-hydroxylation of hm^{6}A through the formation of Schiff base

Mechanism 2.[67]